Michael Meier
michael.meier.1@unil.ch

Carlos Sierra
csierra@bgc-jena.mpg.de

Lausanne, 13.08.2025

To the handling editor – tracked changes

Dear Mr. Sierra,

I am happy to upload all documents for publication. When rereading our manuscript, my co-authors and I felt that some passages could be improved for easier understanding. In addition, we felt that consistency in the usage of the terms ‹simulation› and ‹prediction› should be improved. These improvements have been made and marked with tracked changes in the following main part and supplement of our manuscript.

I hope you may accept these changes and the we can proceed towards the final publication of our study. In the meantime, please do not hesitate if you may need any further information or have any questions.

Best regards,
Michael Meier

Aging and stress explains the earlier start of leaf senescence in trees duringin warmer years: translating the latest findings on senescence regulation into the DP3 model (v1.1)

5   Michael Meier*[1,2], Christof Bigler[23], Isabelle Chuine[1]

[1] CEFE, Univ Montpellier, CNRS, EPHE, IRD, Montpellier, France

[2] Institute of Earth Surface Dynamics, University of Lausanne, Lausanne, Switzerland

[23] Forest Ecology, Department of Environmental Systems Science, ETH Zurich, Zurich, Switzerland

10   *Correspondence to*: Michael Meier, (michael.meier@cefe.cnrs.frmichael.meier.1@unil.ch)

Short summary. The DP3 model of leaf coloring, formulated according to the leaf development process, considerably contrasts previous models and allows to set up new hypotheses, e.g., regarding earlier onset and longer duration of senescence induction and longer senescence predicted for warmer conditions. Comparing the accuracy of the DP3 model to that of previous models and the Null model (average observed date of leaf coloring) suggests that leaf coloring data are noisy, which is why observation protocols and methods should be revised.

Abstract. Leaf senescence ends the growing season of deciduous trees, affecting the amount of atmospheric CO_2 sequestered by forests. Therefore, some climate models integrate projected leaf senescence dates to simulate the carbon cycle. Here, we developed a process-oriented model of leaf senescence (the 'DP3 model') by testing 34 formulations of the leaf development process based on the latest findings on the regulation of leaf aging and senescence. The period between leaf unfolding and leaf senescence was separated into the subsequent young, mature, and old leaf phases, with particular reactions to leaf aging and cold stress, photoperiod stress, and dry stress. The DP3 model predictssimulates daily rates of aging and stress (i.e., separated in cold, photoperiod, and dry stress) along withto predict dates of transition from young to mature to old leaf, senescence induction dates, and leaf senescence dates. This allows new hypotheses regarding the regulation of leaf senescence to be tested. For example, the DP3 model predicted an earlier onset of senescence induction in warmer conditions, likely due to earlier leaf unfolding (aging) and increased cold and dry stress in spring, together with longer-lasting senescence, likely due to the later accumulation of photoperiod stress relative to leaf development and decreased cold stress in summer and fall, which can be validated withthrough experiments and in situ observations. The DP3 model and compared previous models were equally accurate, but less accurate than the Null model (average senescence date observed in the calibration sample). This lower accuracy of the DP3 and compared models is likely due to noise in the visually observed leaf senescence data, which blurs the signal of the leaf senescence process, and to incorrect model formulations. The model errors were similarly affected by climate conditions and location among compared models (including the Null model) and varied mostly due to the leaf senescence data. Noisy leaf senescence data likely force the models to resort to the mean observation, impeding inferences from accuracy-based model comparisons about the leaf senescence process. This calls for revised observation protocols and methods that measure rather than estimate different senescence stages, such as senescence induction and 50% of the leaves have changed color, e.g., based on greenness, involving digital cameras and automated image assessment.

40

1 Introduction

Leaf senescence involves several processes and regulation pathways, but the most important process is the degradation of chlorophyll and breakdown of chloroplasts to retrieve nutrients, especially nitrogen, and to mobilize them in new leaves in spring (Cooke and Weih, 2005; Keskitalo et al., 2005; Lim et al., 2007; Rogers, 2017). A side effect of this nu-
45 trient resorption is the change in leaf color from green to yellow, orange, or red (Keskitalo et al., 2005; but see Wheeler and Dietze, 2023). There have been many studies of how the timing of leaf coloring is influenced by climatic conditions (e.g., Bigler and Vitasse, 2021; Liu et al., 2018; Meier et al., 2021). As these studies usually used the term 'leaf coloring' or 'leaf senescence' to refer to a particular stage of leaf senescence, we use 'leaf senescence' as a collective term for the stages when a given relative amount of leaves have changed color or have fallen, unless stated otherwise.

50 Leaf senescence marks the end of a process that has been better understood over the last ten years, mainly thanks to studies in cell and molecular biology and in environmental sciences ~~(Fig. 1)~~. These studies have shown that leaf senescence relates to leaf development state (e.g., Jan et al., 2019; Jibran et al., 2013; Lim et al., 2007). On the one hand, the development state of leaves depends on their age and thus on the time since leaf unfolding and the state of carbohydrate sinks (Jibran et al., 2013), which relates to photosynthetic activity and nutrient availability (Paul and Foyer,
55 2001). While earlier leaf unfolding was related to earlier leaf senescence (Fu et al., 2014, 2019), an intense discussion has started about the possibility of earlier leaf senescence due to increased photosynthetic activity (Kloos et al., 2024; Lu and Keenan, 2022; Marqués et al., 2023; Norby, 2021; Zohner et al., 2023). On the other hand, the development state of leaves is influenced by hormone levels (Addicott, 1968; Jan et al., 2019; Jibran et al., 2013; Lim et al., 2007), which are, among others, stimulated by environmental stress caused by cold (Kloos et al., 2024; Wang et al., 2022; Xie
60 et al., 2015, 2018), drought (Bigler and Vitasse, 2021; Mariën et al., 2021; Tan et al., 2023; but see Kloos et al., 2024; Xie et al., 2015, 2018), heat (Bigler and Vitasse, 2021; Mariën et al., 2021; Tan et al., 2023; Xie et al., 2015, 2018), heavy rain (Kloos et al., 2024; Xie et al., 2015, 2018), short days (Addicott, 1968; Keskitalo et al., 2005; Singh et al., 2017; Tan et al., 2023; Wang et al., 2022), and lack of nutrients (Fu et al., 2019; Tan et al., 2023). In the early phase of leaf development ('young leaf'), senescence cannot be induced, whereas aging and stress induce it in later phases ('ma-
65 ture leaf' and 'old leaf') and regulate the rate of senescence (**Fig. 1;** Jan et al., 2019; Jibran et al., 2013; Lim et al., 2007; Paul and Foyer, 2001; Tan et al., 2023).
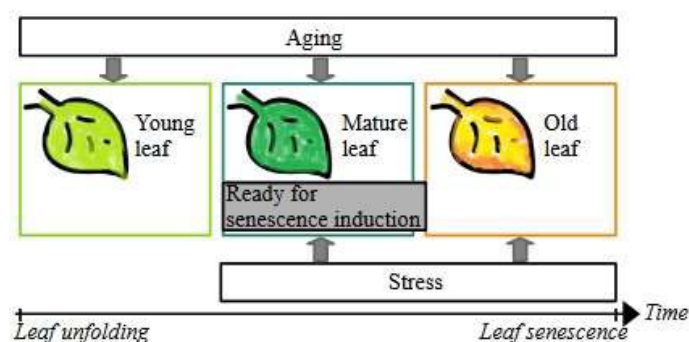

Figure 1. Leaf development. Starting with leaf unfolding, the young leaf develops first into a mature leaf and then into an old leaf. During the three phases of the young, mature, and old leaf, the leaf ages continuously. With the transition from young to mature leaf,

the leaf becomes ready for senescence induction through environmental stress (e.g., cold days). If senescence is not induced through stress in the mature leaf, it certainly is through aging with the transition from mature to old leaf. Thus, senescence cannot be induced during the phase of the young leaf and the ~~date of~~onset of senescence (i.e., the senescence induction date) depends on the time since leaf unfolding and on the environmental conditions since the transition from young to mature leaf. Adapted from Figure 1 in Jibran et al. (2013).

As ~~the timing of~~ senescence induction depends on environmental conditions, leaf senescence of deciduous trees shifts as climate changes, which influences the timing and length of their growing season and thus affects the amount of CO_2 absorbed from the atmosphere (Meier et al., 2021; Menzel et al., 2020; Piao et al., 2019; but see Mariën et al., 2021). This links the feedback loop between atmospheric CO_2 concentration and climate to the feedback loop between climate and forests and more generally to terrestrial ecosystems (Luo, 2007; Richardson et al., 2013). Further, the amount of absorbed CO_2 relates to the amount of sugars available for tree growth, defense, and reproduction (Herms and Mattson, 1992; Tan et al., 2023). Therefore, accurate projections of leaf senescence dates under a changing climate are necessary for accurate forecasts of both climate change and future species composition of temperate forests.

Leaf senescence dates are often projected using process-oriented models. These models are usually based on the results of experiments testing the effect of various environmental cues, that are translated mathematically (Chuine et al., 2013; Chuine and Régnière, 2017). Various process-oriented models of leaf senescence have been proposed over the last twenty years (Liu et al., 2020; Meier and Bigler, 2023). They generally formulate leaf senescence as a one-way process that starts shortly after summer solstice by accumulating a daily rate of senescence until a threshold is reached (but see Wheeler and Dietze, 2023). The daily rate is usually dependent on temperature and day length, and the threshold is either a constant or depends on ~~the timing of~~ leaf unfolding dates, or on environmental conditions~~temperature, precipitation, and photosynthetic activity~~ during the growing season (e.g., Delpierre et al., 2009; Keenan and Richardson, 2015; Liu et al., 2019; Zani et al., 2020).

Previous studies have shown that these leaf senescence models are heavily biased towards the mean of the calibration sample (Meier et al., 2023) and are less efficient relatively to leaf unfolding models (e.g., Liu et al., 2020; Meier and Bigler, 2023). However, it is not yet clear whether this is due to noisy phenological data and/or an incomplete process formulation.

The phenological data used to train leaf senescence models have often been recordings of visual observations, which cover long time periods and are species-specific (e.g., ongoing since 1951 in the Swiss phenology network, 2025). However, the observations are noisy due to different observers and small sample sizes. For leaf senescence, Liu et al. (2021) showed for example that the observer bias was 15 days ~~[d]~~ (d; median) and the sampling bias was 10 d (median) for 10 trees observed per population. These biases not only lead to noise between sites, but also within sites when observers and samples change. Such changes can lead to ~~breaks~~sudden changes in the mean in the time series, as was found for some Swiss sites (Auchmann et al., 2018; Swiss phenology network, 2025). Moreover, the observation protocols may differ between the meteorological institutes and citizen science based networks that are responsible for the recording in the different European countries (Menzel, 2013).

Current models formulate leaf senescence as the result of an accumulated stress caused by cold and short days after summer solstice (Delpierre et al., 2009; Dufrêne et al., 2005; Keenan and Richardson, 2015; Lang et al., 2019; Liu et al., 2019; Zani et al., 2020). Two models further consider environmental conditions before summer solstice, either through temperature and precipitation during the growing season (Liu et al., 2019) or through ~~the~~ photosynthetic activity during the growing season (Zani et al., 2020), while one model considers age through ~~the timing of~~ leaf

unfolding dates (Keenan and Richardson, 2015). However, in these models, environmental conditions and age affect the amount of stress needed for leaf senescence rather than senescence induction. In other words, according to current mod-
els, ~~the~~ senescence induction depends only on stress caused by cold and short days after summer solstice, which consid-
erably contrasts with current knowledge (see above~~; Fig. 1~~). None of the current models allows for senescence induction ~~caused by~~due to aging or stress before summer solstice. While two models consider stress that occurred before summer solstice, senescence is always induced after summer solstice. Finally, we are unaware if aging, stress caused by other than cold and short days, and different stress effects among the phases of leaf development have been tested, as none of the corresponding studies mentioned tested but discarded model formulations.

Here, we developed a new process-oriented model that ~~simulates~~predicts ~~the timing of~~ leaf senescence dates based on the latest knowledge of the physiological processes and drivers of leaf senescence. ~~The timing of l~~Leaf senes-
cence was formulated through a leaf development process that starts at leaf unfolding and is driven by aging and various types of abiotic stress. We tested 34 model formulations of this process. Finally, the most accurate formulation was eval-
uated with a particular focus on the differences between the ~~simulated~~predicted and observed ~~values~~dates (i.e., 'model errors'). We addressed the following research questions:

(1) Which model formulation yields the most accurate ~~simulations~~predictions ~~of the timing~~ of leaf senescence dates?

(2) How accurately does this model ~~simulate~~predict leaf senescence dates compared to previous models?

(3) How do the model errors relate to the phenological data, climate, and site conditions?

2 Data and methods

2.1 Phenological data

The model was developed and evaluated with leaf phenology data of common beech (*Fagus sylvatica*, L.), which was visually observed in Austria, Germany, ~~Switzerland, and~~ Great Britain, and Switzerland between 1950 and 2022 (Fig. 2, Table 1, Sect. S1.1; PEP725, 2024; Swiss phenology network, 2025; Templ et al., 2018). We used the phenological stages 50% of the leaves ~~are~~have unfolded as well as 50% and 100% of the leaves have changed color or have fallen (hereafter referred to as 'leaf unfolding' [LU], 'leaf senescence$_{50}$' [LS$_{50}$], and 'leaf senescence$_{100}$' [LS$_{100}$], respectively; corresponding to BBCH15, BBCH95, and BBCH97 according to Meier, 2018). The LS$_{100}$ data were recorded in Austria and Great Britain only.

We checked all site-years with regards to the order and completeness of the phenological observations. Ob-
servations of LS$_{50}$ and LS$_{100}$ that occurred between the day of year (doy) 60 and 151 were discarded, as were observa-
tions of LU that occurred after doy 180 or after LS$_{50}$ or LS$_{100}$. Thus, we considered only site-years with an observation for LU that was followed by either LS$_{50}$ or LS$_{100}$, or by both LS$_{50}$ and later LS$_{100}$, leaving 5018 sites.

From these sites, we made a pre-selection so that the phenological and geographical range of the LS$_{50}$ obser-
vations was evenly covered and all LS$_{100}$ observations were included. This involved splitting all 5018 sites into 8–10 bins with equal spans for the average and standard deviation of LS$_{50}$ as well as for latitude, longitude, and elevation, so that each bin contained at least two sites (e.g., the range between doy 232 and 328 for the average LS$_{50}$ was split into ten bins of 9.7 days). From each bin, we chose the site with the most LS$_{50}$ observations, with random choice if this applied to more than one site. These sites were completed by all sites with an LS$_{100}$ observation, resulting in a pre-selection of 7137 LS$_{50}$ and 850 LS$_{100}$ observations recorded at 244 and 106 sites, respectively.
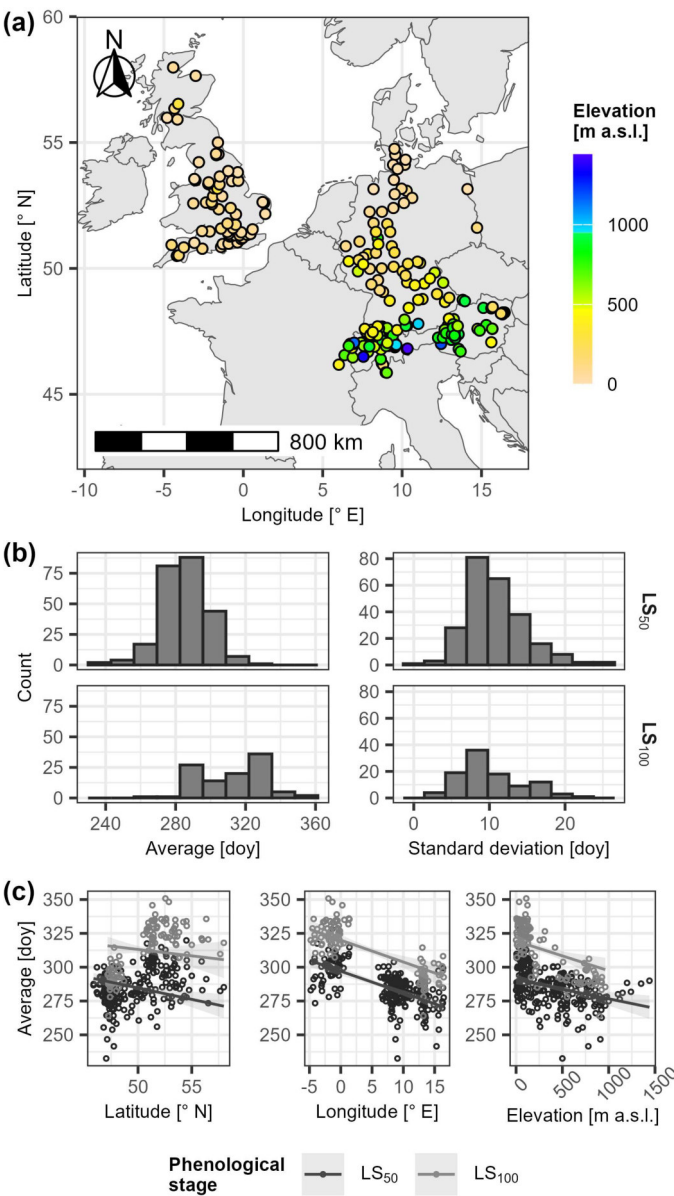
140

Figure 2. Selected phenological sites. Panel (a) locates the selected sites and indicates corresponding elevation [meters above sea level (m a.s.l.)]. In (b), the histograms illustrate the distributions of the site-specific average day of year (doy; left) and corresponding standard deviation (right) per leaf senescence stage ~~(~~[i.e., 50% and 100% of the leaves have changed color or have fallen ~~(~~(LS$_{50}$ and LS$_{100}$, respectively~~)~~]; rows~~)~~]. Panel (c) plots the site-specific average ~~day of year~~doy of LS$_{50}$ and LS$_{100}$ (grey and black circles, respectively) in relation to site latitude [°N] (left), longitude [°E] (middle), and elevation [m a.s.l.] (right), together with the linear regression lines and corresponding 99% confidence intervals. The linear regression explained ~~S~~site-specific average LS$_{50}$ and average LS$_{100}$ ~~were explained~~ by latitude, longitude, and elevation (Sect. S1.1.2) ~~and c~~. Corresponding estimates were plotted against latitude~~,~~ for mean longitude and mean elevation (left), against longitude~~,~~ for mean latitude~~,~~ and mean elevation (middle), and against elevation~~,~~ for mean latitude~~,~~ and mean longitude.

Table 1. Observations of spring and ~~autumn~~fall leaf phenology.

Stage	Country	Sites	Total number of site-years (min.–max. per site)	Observation period	Range of observations [doy]	Source
LS$_{50}$	Austria	51	1011 (5–54)	1950–2015	209–321	PEP725
	Germany	68	3238 (14–65)	1951–2015	196–331	PEP725
	Great Britain	64	303 (2–6)	1999–2005	258–337	PEP725

	Switzerland	61	2585 (6–72)	1951–2022	197–344	SPN
LS$_{100}$	Austria	43	578 (1–34)	1950–1986	263–335	PEP725
	Great Britain	63	272 (1–6)	1999–2005	286–365	PEP725
LU	Austria	51	1020 (5–54)	1950–2015	80–166	PEP725
	Germany	68	3238 (14–65)	1951–2015	80–175	PEP725
	Great Britain	64	331 (5–6)	1999–2005	85–140	PEP725
	Switzerland	61	2585 (6–72)	1951–2022	67–161	SPN

Note: LU refers to the stage when 50% of the leaves are unfolded. LS$_{50}$ and LS$_{100}$ refer to the stages when 50% and 100% of the leaves, respectively, have changed color or have fallen. The timing of these stages is given by the day of year (doy). A site-year is a year for which an observation of both LU and LS$_{50}$ or LS$_{100}$ was recorded at a given site. Two data sources were considered: PEP725 (Templ et al., 2018) and the Swiss phenological network (SPN; Swiss phenology network, 2025).

2.2 Driver data

For each phenological site, weather variables, elevation, and the leaf area index (LAI) were approximated by the weighted averages from octagons with a radius of 2.5 km around the phenological sites, and combined with the atmospheric CO_2 concentration. Daily weather variables and elevation were derived for each site from the E-OBS dataset (Copernicus Climate Change Service, Climate Data Store, 2020; Cornes et al., 2018), which contains interpolated data from a 100-member ensemble driven with meteorological observations. We extracted and approximated site elevation, maximum temperature, mean temperature, minimum temperature, precipitation, relative humidity, and surface shortwave down welling radiation for 1950–2022. These temperature variables were corrected through day- and site-specific lapse rates to account for elevational differences between the octagon averages and sites (i.e., the elevation according to the phenology datasets or, if missing, according to EU-DEM, 2024, with a resolution of 25 m, and the location according to the phenology datasets). These laps rates were linearly regressed from the grid cell of a particular site and the eight neighboring grid cells, assuming an elevation of 0 meters above sea level (m a.s.l.) for grid cells over the sea. Occasional gaps in the regressed lapse rates were interpolated with site-specific cubic splines. LAI per site was taken from the remote sensed monthly LAI (1981–2015) in the GIMMS-LAI3g dataset (version 2; Mao and Yan, 2019). LAI is averaged among years in this dataset, and thus we also used these monthly LAI values for the years 1950–1980. Atmospheric CO_2 concentrations were taken from a reconstructed dataset for the years ~~and a remote sensed dataset for the years~~ 1950–2013 and a remote sensed dataset for the years 2002–2022~~, respectively~~ (Cheng et al., 2022; Copernicus Climate Change Service, Climate Data Store, 2018). Both datasets provide monthly data, which we distilled into annual averages. These averages were combined through weighted means over the years 2002–2013 to assure a smooth transition between the datasets. As some monthly CO_2 observations between 2002–2022 were missing, we used modeled CO_2 values derived from site-specific cubic splines based on the remote sensed data (Copernicus Climate Change Service, Climate Data Store, 2018).

We further calculated for each site day length, daily photosynthetic activity, and the daily Keetch and Byram drought index (KBDI). Day length was calculated following Brock (1981), using the latitude of each site (Sect. S1.2.1). Daily sink limited photosynthetic activity was calculated following Farquhar et al. (1980) and Collatz et al. (1991), using daily surface shortwave down welling radiation, day length, and mean temperature together with monthly LAI averaged among years and annual~~monthly~~ atmospheric CO_2 concentration ~~as well as monthly LAI averaged among years~~ (Sect. S1.2.2). The daily KBDI was calculated following Keetch and Byram (1968), using precipitation and maximum temperature (Sect. S1.2.3).

170 **2.3   Model conceptualization**

Based on the process of leaf development according to Jibran et al. (2013), we defined our model as a one-way process that may be formulated with either two or three phases of leaf development, namely either the phases mature and old leaf or the phases young, mature, and old leaf (Figs. 1 and 3). After leaf unfolding, the young leaf is insensitive to stress and ages until it becomes a mature leaf (Fu et al., 2014; Jibran et al., 2013; Keenan and Richardson, 2015). The mature

175 leaf can be affected by stress and ages until it becomes an old leaf ~~–~~(Jan et al., 2019; Jibran et al., 2013; Lim et al., 2007). Senescence induction may be ~~induced~~caused by stress in the mature leaf or by aging, in the case of which it coincides with the transition from mature to old leaf, causing the leaf to change color and to fall off (Jan et al., 2019; Jibran et al., 2013; Lim et al., 2007).
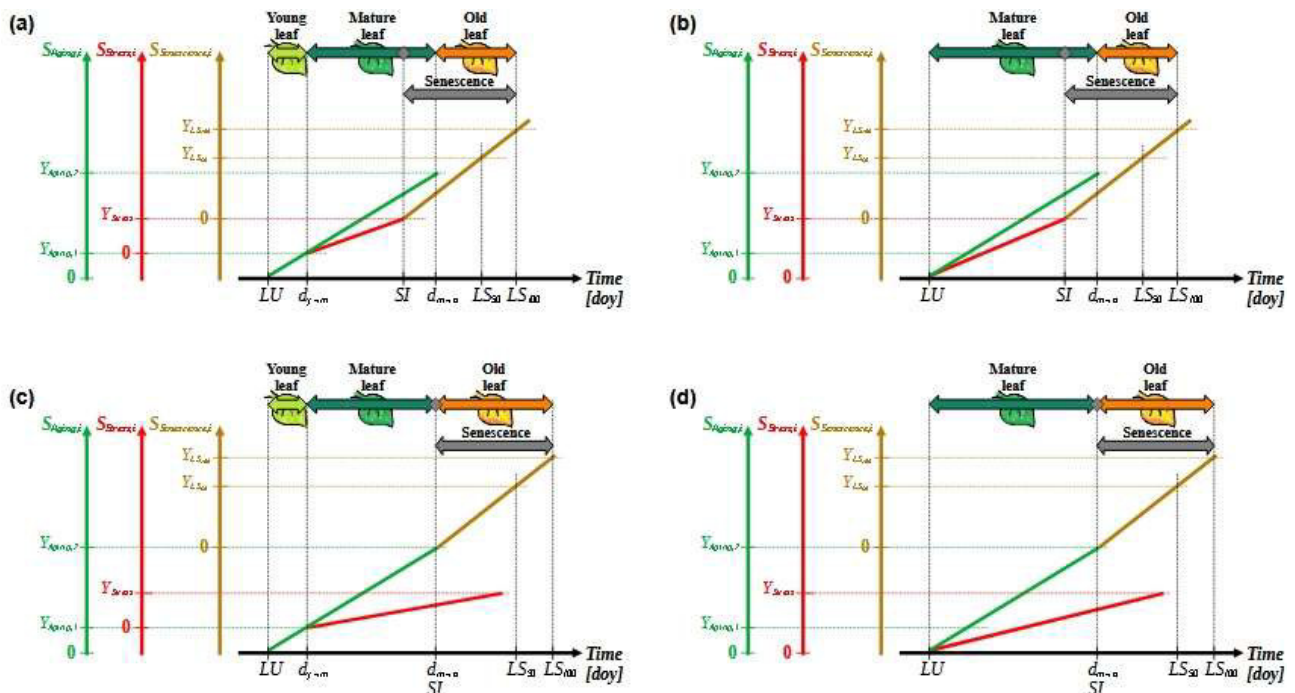

Figure 3. Conceptualization of the leaf development model. The process of leaf development is defined by three subsequent phases of leaf development, i.e., 'young leaf', 'mature leaf', and 'old leaf' [light green, dark green, and orange horizontal arrows, respectively; panel (a) and (c)]. Alternatively, the process is simplified into two subsequent development phases, i.e., 'mature leaf', and 'old leaf' (panel b and d). Senescence may be induced by stress during the phase of the mature leaf [grey rhombuses; panels (a) and (b)] or by aging on the day of transition from the mature to the old leaf [$d_{m\to o}$; panels (c) and (d), respectively]. The state of aging, stress, and senescence (y-axes; $S_{Aging,i}$, $S_{Stress,i}$, and $S_{Senescence,i}$; Eq. 1; solid green, red, and brown lines, respectively) for day i are derived from the corresponding daily rates (Eqs. 3, 4, and 8) accumulated over time (~~(~~[x-axis; day of year ~~[~~(doy)]~~)~~). Starting from the ~~day of~~ leaf unfolding date (LU), these states simulate the leaf development, marked by transitions from the young to the mature leaf ($d_{y\to m}$) and ~~from the mature to the old leaf (~~$d_{m\to o}$ as well as by the dates of senescence induction (SI) and of the phenological stages 50% and 100% leaf coloring or fall (LS_{50} and LS_{100}, respectively). These transitions and stages occur when $S_{Aging,i}$, $S_{Stress,i}$, and $S_{Senescence,i}$ ~~b~~reach corresponding thresholds ($Y_{Aging,1}$, $Y_{Aging,2}$, Y_{Stress}, Y_{LS50}, and Y_{LS100}). SI is defined as the first day on which either Y_{Stress} or $Y_{Aging,2}$ is ~~b~~reached [panels (a) and (b) versus panels (c) and (d), respectively] and marks the ~~beginning~~onset of senescence (grey horizontal arrow), during which the daily senescence rate accumulates. If SI results from ~~the breach of~~ $Y_{Aging,2}$ ~~,~~ being reached, it coincides with $d_{m\to o}$. Dotted lines are auxiliary lines.

180   ~~We constructed and tested the formulations of~~Based on these definitions, we formulated the leaf development process under ~~(see Sect. 2.2.3) by combining the~~ following assumptions. ~~We considered that a~~Aging ~~could~~may be ~~mod-eled~~simulated either by photosynthetic activity (Jibran et al., 2013; Paul and Foyer, 2001; Zohner et al., 2023) or more simply by a number of days. Stress may be ~~modeled~~simulated by a combination of sudden or gradual responses to the

stressors cold, shortening day length, drought, heat, frost, heavy rain, and nutrient depletion (Bigler and Vitasse, 2021; Jan et al., 2019; Jibran et al., 2013; Kloos et al., 2024; Mariën et al., 2021; Tan et al., 2023; Wang et al., 2022; Xie et al., 2015, 2018; Zohner et al., 2023). ~~Finally, we considered that leaf s~~Senescence may be simulated in linear, convex, or sigmoidal dependence on combined~~could result as a combination of~~ aging and stress (Tan et al., 2023; Xie et al., 2015).

All formulations are based on daily states of aging, stress, and senescence (Eq. 1), which are compared to corresponding thresholds (Eq. 2):

$$S_{k,j} = \sum_{i=t_{0,k}}^{j} R_{k,i} \tag{1}$$

$$S_{k,j} \geq Y_k \tag{2}$$

Here, $S_{k,j}$ is the state on day j of either aging, stress, or senescence (k). ~~that are~~This state is formulated as the sum of the corresponding rates on day i ($R_{k,i}$), which accumulated between the starting day $t_{0,k}$ and j, until the threshold Y_k is reached. In other words, the daily aging rate ($R_{Aging,i}$) accumulates from LU ($t_{0,Aging}$ = LU). The transition from young leaf to mature leaf occurs when $S_{Aging,j}$ reaches $Y_{Aging,1}$. Thus, day j becomes $t_{0,Stress}$ and the accumulation of the daily stress rate ($R_{Stress,i}$) starts, while $R_{Aging,i}$ continues to accumulate. While the transition from mature leaf to old leaf occurs when $S_{Aging,j}$ reaches $Y_{Aging,2}$, senescence is either induced with this transition or already earlier due to $S_{Stress,j}$ reaching Y_{Stress}. Upon senescence induction, day j becomes $t_{0,Senescence}$ and the daily senescence rate ($R_{Senescence,i}$) starts to accumulate. Eventually, $S_{Senescence,j}$ reaches $Y_{LS_{50}}$ and $Y_{LS_{100}}$, and respective LS$_{50}$ and LS$_{100}$ are marked by the corresponding days j.

$R_{Aging,i}$ was either set equal to the daily net photosynthetic activity or to one (i.e., A_{net} [mol C d^{-1}] or 1 [d d^{-1}], respectively), depending on the formulation (Eq. 3):

$$R_{Aging,i} = \begin{cases} A_{net,i} \\ 1 \end{cases} \tag{3}$$

$R_{Stress,i}$ was formulated as the sum of three to seven weighted stressors (D_{stress}; Eqs. 4–6), always considering (1) cold days (derived from minimum temperature; Tn [°C]), (2) shortening days (derived from the difference in day length; δL [h], with $\delta L_i = L_i - L_{i-1}$), and (3) dry days (approximated by ~~the Keetch and Byram drought index [KBDI~~; Q). In addition, some formulations of R_{Stress} also considered (4) periods of heavy rainfall (approximated by the five-days precipitation; $P5$ [mm], with $P5_i$ being the sum of P_{i-4} to P_i~~to P_{i-4}~~), (5) heat days (derived from maximum temperature; Tx [°C]), (6) nutrient depletion (approximated by the accumulated A_{net} since LU, due to the absence of soil data), and/or (7) frost days (through a response to Tn with~~derived from~~ lower ~~minimum temperature~~thresholds than for cold days; Table S3~~; Tn [°C]~~):

$$R_{Stress,i} = \sum w_{D_{Stress}} \times f(D_{Stress,i}) \tag{4}$$

$$D_{Stress,i} \in \left\{ Tn_i, \quad \delta L_i, \quad Q_i, \quad P5_i, \quad Tx_i, \quad \sum_{l=d_{LU}}^{i} A_{net,l}, \quad Tn_i \right\} \tag{5}$$

$$f(x)=\begin{cases}g(x)\\h(x)\end{cases} \tag{6}$$

Here, $w_{D_{Stress}}$ is the weight for the response $[f(x)]$ to D_{Stress}, calculated according to $g(x)$ or $h(x)$ (Eqs. 7 and 8):

225
$$g(x)=\begin{cases}1 &, & if\ x\geq a\\0 &, & if\ x<a\end{cases} \tag{7}$$

$$h(x)=\begin{cases}1 &, & if\ x<b_0\\\dfrac{b_1-x}{b_1-b_0} &, & if\ b_0\leq x\leq b_1\\0 &, & if\ x>b_1\end{cases} \tag{8}$$

While a marks the sudden boundary between an unstressed and stressed state, b_0 and b_1 mark the lower and
230 upper bounds, respectively, between which stress gradually increases (Fig. 4). Because stress results when $x \geq a$ and
$x \geq b_0$ ~~result in stress~~, the response to δL and Tn was formulated as $g(-\delta L)$ and $g(-Tn)$ as well as $h(-\delta L)$ and $h(-Tn)$~~;~~. This
~~which~~ translates in stress if $\delta L \leq -a$ ~~∨~~, $\delta L \leq -b_0$ ~~and~~, $Tn \leq -a$, and ~~∨~~ $Tn \leq -b_0$. For example, if stress occurs suddenly or
gradually when $\delta L \leq -0.01$ h, then $a = 0.01$ h ~~or~~and $b_0 = 0.01$ h, respectively. Note that these are examples, see Table 3
for the calibrated values.

235
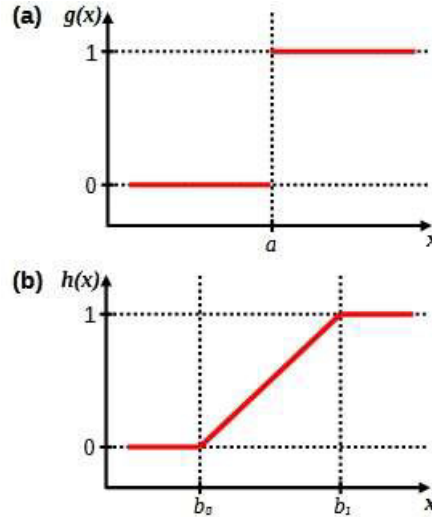
Figure 4. Response functions (solid red lines) of $g(x)$ and $h(x)$. In (a), a marks the boundary value of x at which $g(x)$ suddenly
changes from 0 to 1 (i.e., from no effect to an effect). In (b), b_0 and b_1 mark the lower and upper bounds of x, respectively, between
which $f(x)$ gradually increases from 0 to 1. Dotted lines are auxiliary lines.

$R_{Senescence,i}$ was either formulated as the sum, product, or exponential function of $R_{Aging,i}$ and $R_{Stress,i}$ or of $S_{Aging,i}$
and $R_{Stress,i}$, which yield linear, convex, and sigmoid curves, respectively (Eq. 9):

$$R_{Senescence,i} = \begin{cases} w_A R_{Aging,i} + w_S R_{Stress,i} \\ s_X \left(R_{Aging,i} \times R_{Stress,i}^{x_S} \right) \\ s_X \dfrac{1}{e^{c\, S_{Aging,i}(d - R_{Stress,i})}} \end{cases} \tag{9}$$

w_A and w_S are the weights of R_{Aging} and R_{Stress}, respectively, and s_X is a scaling factor, all of which allowed us to hard code $Y_{LS_{50}} = 1$, x_S is the range bounded exponent of R_{Stress}, while c and d are the parameters of the sigmoid curve that relates R_{Stress} and S_{Aging} (Lang et al., 2019).

2.4   Model calibration and validation

We selected the observations for the calibration and validation samples with different procedures. To have a low risk of overfitting (i.e., the bias–variance trade-off; Sect. 2.2.2 in James et al., 2017), each calibration sample contained at least ten observations per calibrated parameter (Meier and Bigler, 2023). We defined two calibration datasets: one to calibrate a model that ~~simulates~~predicts both LS_{50} and LS_{100} simultaneously, and one to calibrate a model that ~~simulates~~predicts LS_{50} only. For the two datasets, we ~~selected~~identified the site-years ~~from those~~ with the most extreme conditions during the growing season, i.e., the hottest, coldest, driest ten day periods observed between LU and LS_{50} as well as the shortest and longest growing season observed in the pre-selected data (Sect. 2.1). For the first dataset, hereafter called 'LS_{50}-LS_{100} sample', we randomly selected 250 of these site-years containing an observation for both LS_{50} and LS_{100}. For the second dataset, hereafter referred to as 'LS_{50} sample', we randomly selected 250 of these site-years containing observations for LS_{50}. These calibration samples were paired with validation samples that contained all remaining LS_{50} and LS_{100} observations or all remaining LS_{50} observations, respectively. We drew twice both the LS_{50} and LS_{50}-LS_{100} samples. While model development was based on the LS_{50}-LS_{100} samples, model evaluation was based on the LS_{50} sample to allow for a comparison with previously published models. All models were calibrated five times per drawn sample (i.e., ten 'calibration runs' per model and LS_{50} sample or LS_{50}-LS_{100} sample) by minimizing the root mean squared error (RMSE; Eq. S44) with generalized simulated annealing and optimal, model-specific controls (see Sect. S2.2; Xiang et al., 1997, 2017).

2.5   Model development

We based our model on the most accurate formulation of the leaf development process after testing different formulations in several iterations (Fig. 5; see Table S3 for parameter ranges). First, we defined the process structure based on sudden responses [$g(x)$; Eq. 7] to the stressors for cold days, shortening days, and dry days ~~transformed through threshold response functions [g(x); Eq. 7]~~. In iteration 1, we tested the definition of the aging rate (R_{Aging}) and of the senescence rate ($R_{Senescence}$) based on the two phases of leaf development 'mature leaf' and 'old leaf' (Figs. 3b and 3c). R_{Aging} was formulated as a function of either the net photosynthetic activity (A_{net}) or of the number of days (Eq. 3). $R_{Senescence}$ was formulated in linear, convex, or sigmoidal dependence on combined~~as a combination of~~ aging and stress [through R_{Aging} or the state of aging (S_{Aging}) and through the stress rate (R_{Stress})] in either a sum, product, or exponential function (Eq. 9). In iteration 2, we tested the number of phases of leaf development and added the ~~, i.e., either two phases 'mature leaf' and 'old leaf', or three~~ phase~~s~~ 'young leaf' (Figs. 3a and 3d)~~, 'mature leaf', and 'old leaf'~~. Thus, we formulated R_{Stress} with with gradual responses [$h(x)$; Eq. 8] to the initial stressors and a forward selection of additional stressors ~~and selecting between g(x) and gradual response functions [h(x); Eq. 8]~~. In iteration 3, we considered each stressor

for cold days, shortening days, and dry days through $h(x)$ rather than $g(x)$. In iteration 4, we considered one additional stressor, i.e.~~,~~ heavy rain periods, heat days, nutrient depletion, or frost days through $g(x)$. In iteration 5, we considered the additional stressor through $h(x)$ rather than $g(x)$. In iteration 6, the procedure of iterations 4 and 5 was repeated as long as they resulted in a formulation that was selected for further development.

The formulations to be further developed were selected according to the accuracy of the corresponding model in ~~simulating~~predicting LS_{50} and LS_{100}, i.e., through calibration with the LS_{50}-LS_{100} sample. This accuracy was assessed with the Akaike information criterion corrected for small samples (AICc; Eq. S41; Akaike, 1974; Burnham and Anderson, 2004), which accounts for both the goodness-of-fit between the ~~simulated~~predicted and observed ~~values~~leaf senescence dates and the number of free parameters. ~~We calculated t~~The AICc was calculated for each calibration run (see Sect. 2.4) and ~~excluded~~the run with the highest AICc per model was excluded. We further developed the formulations of~~, before identifying~~ the two models with the lowest median AICc across the given and all previous iterations. Finally, ~~we selected~~the model ~~based on the formulation~~with the lowest median AICc was selected and~~, which was~~ further evaluated.

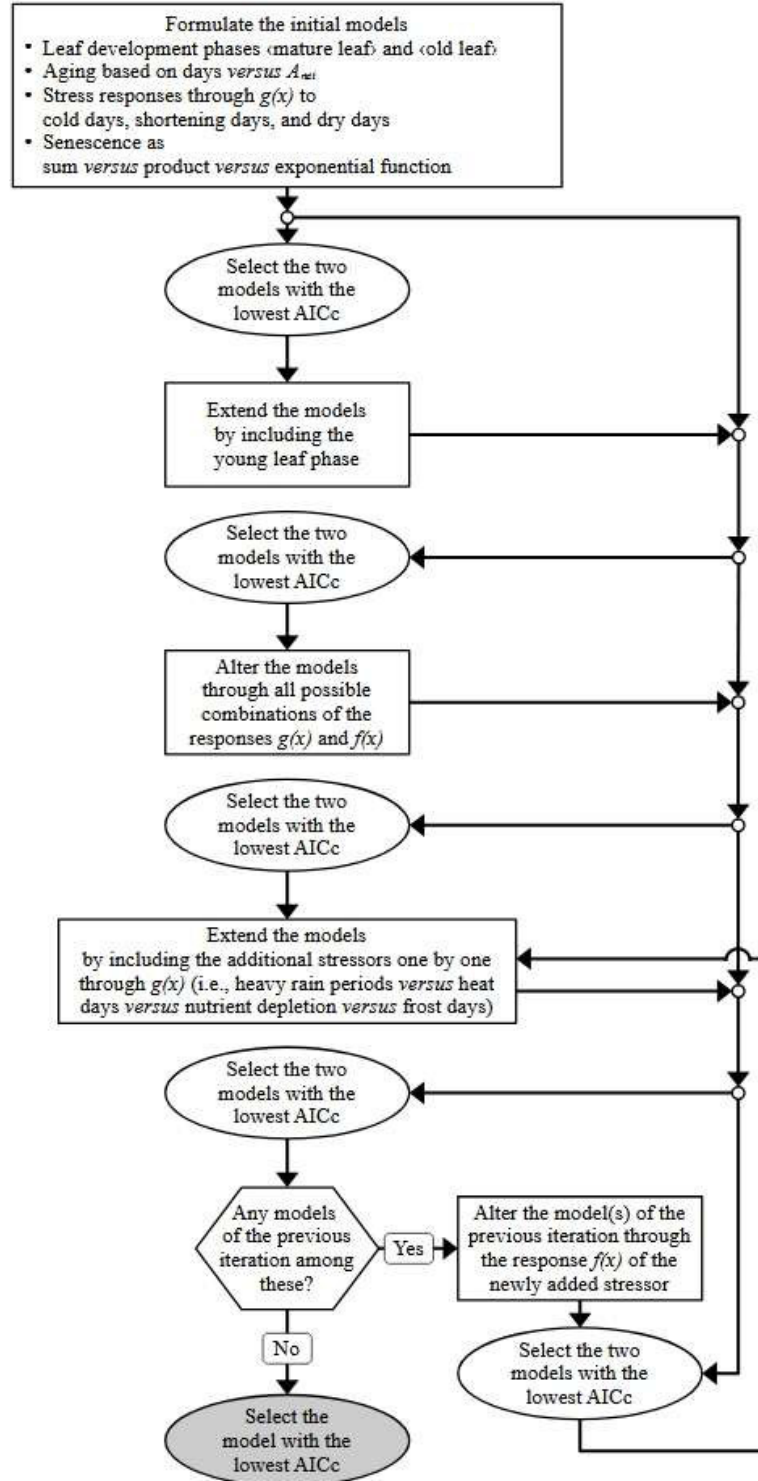**Figure 5. Model development.** The iterations of model development are symbolized with rectangles. Selection of the best formulated models (ellipses) was based on the Akaike information criterion corrected for small samples (AICc; Eq. S41; Akaike, 1974; Burnham and Anderson, 2004) and the final selection is marked grey. For the response function~~s to the stressors, i.e.,~~ $g(x)$ and $h(x)$, see Eqs. 7 and 8.

2.6   Model evaluation

First, we evaluated the functionality of the selected model. We were particularly interested in the causes of senescence induction that could be due to aging or stress (Fig. 3). We counted how often aging versus stress induced senescence, and we quantified the relative amount of accumulated stress caused by each stressor at the time of senescence induction. We compared both aging- and stress-induced senescence as well as the relative amounts of stress across mean annual temperature (MAT; °C), mean annual KBDI (MAQ), latitude (LAT; °N), and elevation (ELV; m a.s.l.) for the given year and site. While MAT and MAQ ~~are~~were assumed to directly affect cold and dry stress, LAT relates to day length through the inclination angle of the Earth **(Brock, 1981)**, and ELV relates to dry stress through decreasing nutrients with elevation (Huber et al., 2007; Loomis et al., 2006). The evaluation was based on the calibration runs that resulted in the highest modified Kling-Gupta efficiency (KGE'; Eq. S45; Gupta et al., 2009; Kling et al., 2012), which combines bias, variability, and correlation of the ~~simulated~~predicted and observed leaf senescence dates.

Second, we compared the accuracy between the selected model and three previously published models, namely the CDD, DM2, and PIA model. Because these models simulate only one stage of leaf senescence, which usually is LS_{50}, we based our comparison on this stage (Delpierre et al., 2009; Dufrêne et al., 2005; Zani et al., 2020). The CDD model determines LS_{50} by the time the cold degree-days reaches a particular threshold (Dufrêne et al., 2005). The DM2 model accumulates the product of temperature differences and day length ratios to corresponding thresholds until the threshold that determines LS_{50} is reached (Delpierre et al., 2009). The PIA model accumulates temperatures and day lengths that are combined in an exponential function, and derives the threshold to determine LS_{50} from the photosynthetic activity during the growing season (Zani et al., 2020). All these models were compared based on the calibration run that resulted in the highest KGE'. Further, we compared the RMSE and AICc as well as the Pearson correlation (ρ) across the entire validation sample (ρ_{Overall}), across space (ρ_{Spatial}), and across time (ρ_{Temporal}). ρ_{Spatial} was calculated across sites based on ~~the site specific~~their mean predicted and observed ~~and simulated~~ LS_{50} ~~across sites~~. ρ_{Temporal} was calculated for each site, based on the yearly predicted and observed ~~and simulated~~ LS_{50}.

Third, we estimated the extent to which the model error (i.e., ~~simulated~~predicted minus observed LS_{50}) was affected by data structure as well as by climatic and spatial deviations from the LS_{50} calibration sample, using a linear mixed-effects model (LMM; Pinheiro and Bates, 2000) and an analysis of variance (ANOVA; Sect. S2.4; Fox, 2016). In the LMM, the response variable 'model error' was explained by the factor variable 'country' as well as the interaction of the factor variable 'model' with each of the differences between a site-year and the average of the calibration sample in MAT (δMAT), MAQ (δMAQ), the accumulated A_{net} between LU and summer solstice (δA_{net}), latitude (δLAT), and elevation (δELV). The random intercept was grouped by 'site'. The LMM was fitted with fast restricted maximum likelihood (Wood, 2011), and served as basis for ~~an~~the ANOVA. This type-III ANOVA (Yates, 1934) quantified the impact of the explanatory variables ~~in~~on the variance of the model error that was explained by the LMM. The impact attributable to data structure was caused by the fixed effects of 'country' and the standard deviation in the random intercepts grouped by 'site', while the impacts attributable to climatic versus spatial deviations from the calibration sample was caused by the effects of δMAT, δMAQ, and δA_{net} versus the effects of δLAT and δELV, respectively.

2.7   Statistical software and reporting of results

We used the programming language R, together with the R package data.table for data processing (Barrett et al., 2024). In R, data from xslx files were extracted with the R package readr (Wickham et al., 2024), and data from netCDF files were extracted and averaged with the R packages ncdf4 (Pierce, 2023), raster (Hijmans, 2023), sf (Pebesma, 2018;

Pebesma and Bivand, 2023), and sp (Bivand et al., 2013; Pebesma and Bivand, 2005). Leap years were identified with the function leap_year in the R package lubridate (Grolemund and Wickham, 2011). Gaps in the regressed lapse rates were filled with the function na.spline in zoo (Zeileis and Grothendieck, 2005). Seasonal splines of atmospheric CO_2

330 concentrations were calculated with the function sm in npreg (Helwig, 2024). The leaf senescence models were calibrated with the R package GenSA (Xiang et al., 2013), while the LMM was fitted with the R package mgcv (Wood, 2017) and the ANOVA was calculated with the R package stats (R Core Team, 2025). LMM estimates and 99% confidence intervals (i.e., significance level $\alpha = 0.01$) for combined coefficients, e.g., the effect of δMAT for a given model, were calculated with the Delta method (Chpt. 5.1.4 in Fox and Weisberg, 2019; Chpt. 9.9 in Wasserman, 2004) through

335 the function deltaMethod in the R package car (Fox and Weisberg, 2019). For each LMM coefficient and ANOVA impact, we expressed the most optimistic change of odds between the null hypothesis (being zero; H_0) and alternative hypothesis (being different from zero or greater than zero, respectively; H_1) with the minimum Bayes factor (BF$_{01}$), labeling H_0:H_1 ratios of 1/1000 and 1/100 as 'decisive' and 'very strong', respectively (Held and Ott, 2018; Johnson, 2005). BF$_{01}$ was calculated from the p-values and number of data with the function tCalibrate in the R package pCalibrate

340 (Held and Ott, 2018). For the visualizations, we used the R packages ggplot and ggpubr (Kassambara, 2020; Wickham, 2016), as well as the R packages ggspatial and rnaturalearth for the maps (Dunnington, 2023; Massicotte and South, 2023).

3 Results

3.1 Model formulation – the DP3 model

We tested 34 formulations of the leaf development process through 1428 calibration runs, and found that three subse-

345 quent leaf development phases resulted in the most accurate model (according to the AICc; Figs. 3a, 3c, 6 and S1–S2). In this model, the phase 'young leaf' starts with leaf unfolding. As a daily aging rate R_{Aging} accumulates (Eq. 10), the simulated state of aging increases by one day per day. When this state reaches the threshold $Y_{Aging,1}$ (Eqs. 1 and 2), the phase 'mature leaf' begins. During this phase, the leaf continues to age and is also sensitive to stress caused by cold days, shortening days, and dry days, to which we hereafter refer to as 'cold stress', 'photoperiod stress', and 'dry stress',

350 respectively. This stress is summarized in a daily stress rate (R_{Stress}; Eq. 11) and thus accumulated to determine the state of stress. The first day that either the state of stress or the state of aging reaches the respective thresholds Y_{Stress} or $Y_{Aging,2}$ (Eqs. 1 and 2), senescence is induced, while the phase 'old leaf' starts only when the state of aging reaches $Y_{Aging,2}$. Once senescence is induced, a daily senescence rate ($R_{Senescence}$) in convex dependence on stress accumulates (Eq. 12) and determines the state of senescence. The days this state reaches the thresholds Y_{LS50} and Y_{LS100} (Eqs. 1 and 2) correspond to

355 the ~~simulated~~predicted dates of LS$_{50}$ and LS$_{100}$, respectively. Hereafter, we refer to this model as 'DP3' model (Tables 2 and 3; Meier, 2025b, coded in R).

$$R_{Aging,i} = 1 \tag{10}$$

360

$$R_{Stress,i} = w_C\, g(-Tn_i) + w_P\, g(-\delta L_i) + w_D\, g(Q_i) \tag{11}$$

$$R_{Senescence,i} = s_X\, R_{Stress,i}^{x_S} \tag{12}$$

Here, w_C, w_P, and w_D are the weights for the response functions $g(x)$ (Eq. 7) to the minimum temperature (Tn), difference in day length (δL), and ~~the Keetch and Byram drought index~~KBDI (Q) on day i, respectively [e.g., $w_P\ g(-\delta L_i)$ results in the photoperiod stress on day i]. s_X is the scaling factor for R_{Stress}, which is 'shaped' by x_S.
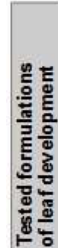

Figure 6. Tested model formulations. The tested formulations differed in their number of leaf development phases (i.e., two or three phases), in their driver of the aging rate ~~(~~[i.e., days or photosynthetic activity ~~[~~(A_{net})~~]~~], their stress rate in response ~~(~~[i.e., $g(x)$ or $h(x)$~~)~~] to the stressors cold, shortening, dry, heat, and frost days, heavy rain periods, and nutrient depletion, and their ~~response~~dependence of the senescence rate ~~to increasing~~on ~~aging~~age and stress (i.e., linear, convex, ~~and~~or sigmoid ~~increase~~dependence as a the result of a sum, product, or exponential function, respectively). After each iteration, we identified the two most accurate formulations across the given and all previous iterations (Fig. 5, Sect. 2.5). These formulation were further developed through the next iteration. As soon as an iteration did not produce any new model formulations, we selected the more accurately formulated model ('top formulation'; i.e., the 'DP3' model). All formulations were tested for beech based on the LS_{50}-LS_{100} sample (Sect. 2.4).

Table 2. Input and output variables of the DP3 model

	Collective list	Name	Definition	Unit	Format
Input	-	*par*	Model parameters (see Table 3)	-	Vector
	data	*LU*	Observed ~~timing of~~leaf unfolding dates	doy	Vector
		id	Unique identifier of each '*LU*' (character)	-	Vector

		D_i	Daily number of days (i.e., 1 per day)	-	Matrix
		Tn_i	Daily minimum temperature	°C	Matrix
		δL_i	Daily difference in day length to previous day	h	Matrix
		Q_i	Daily Keetch and Byram drought index	-	Matrix
	-	*stages*	Leaf senescence stages to be predicted (character, defaults to $LS_{Default}$)	-	Vector
Output	-	*LS*	~~Simulated~~Predicted leaf senescence dates, including senescence induction *(SI)*	doy	Matrix
	transitions	$d_{y \to m}$	~~Simulated~~Predicted timing of transition from young to mature leaf	doy	Vector
		$d_{m \to o}$	~~Simulated~~Predicted timing of transition from mature to old leaf	doy	Vector
	aging	$R_{Aging,i}$	Daily rate of aging	-	Matrix
		$S_{Aging,i}$	State of aging (i.e., accumulated $R_{Aging,i}$ since LU)	-	Matrix
	stress	$X_{Cold,i}$	Daily cold stress [i.e., $w_C\ g(–Tn_i)$]	-	Matrix
		$X_{Photoperiod,i}$	Daily photoperiod stress [i.e., $w_P\ g(–\delta L_i)$]	-	Matrix
		$X_{Dry,i}$	Daily dry stress [i.e., $w_D\ g(–Q_i)$]	-	Matrix
		$R_{Stress,i}$	Daily rate of stress	-	Matrix
		$S_{Stress,i}$	State of stress (i.e., accumulated $R_{Stress,i}$ since $d_{\sim m y \to o m}$)	-	Matrix
	senescence	$R_{Senescence,i}$	Daily rate of senescence	-	Matrix
		$S_{Senescence,i}$	State of senescence (i.e., accumulated $R_{Senescence,i}$ since $\underline{SI}\sim d_{m \to o}$)	-	Matrix

Note: Daily variables refer to day i, and accumulated variables refer to the period until day i. The vector ***par*** contains the model parameters listed in Table 3. In the collective lists data, aging, stress, and senescence, the rows of the matrices refer to the days of the year, while the columns refer to site-years and are ordered identically between all matrices. ~~The~~This order ~~of these matrix columns~~ matches the order of the vectors in the collective lists data and transition. For the ***LS*** matrix, the rows refer to the site-years and the columns refer to the senescence induction date ~~(SI)~~ and the dates of the leaf senescence stages indicated by the vector ***stages***. *LU, LS,* $d_{y \to m}$, and $d_{m \to o}$ are given in day of year (**doy;** Meier, 2025b).

Table 3. Fitted parameters of the DP3 model

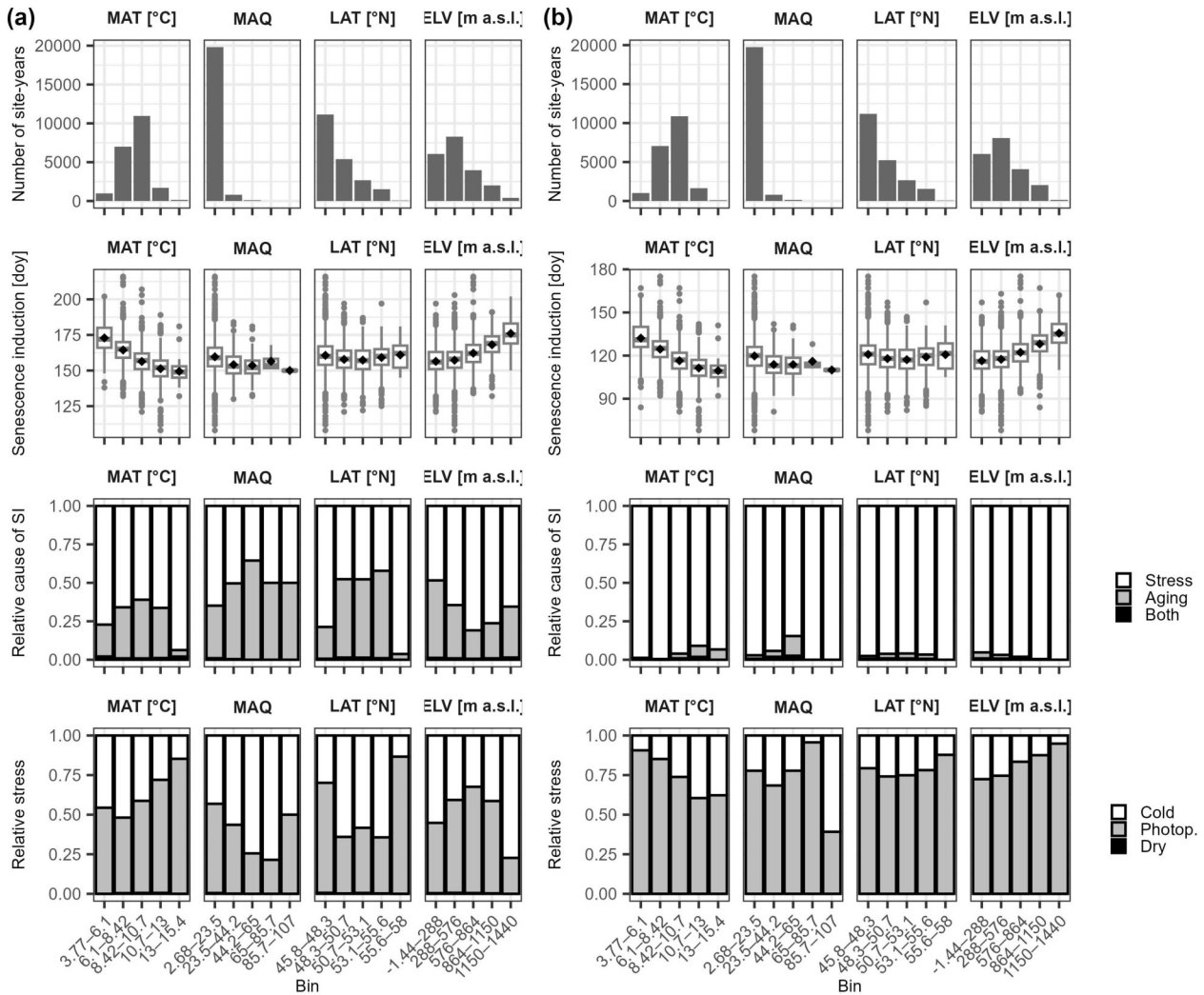|		Fitted value	
Parameter	Meaning	LS_{50}-LS_{100}	LS_{50}
$–a_C$	Boundary below which cold stress is 1 versus 0 (referring to Tn_i)	2.55 °C	0.06 °C
$–a_P$	Boundary below which photoperiod stress is 1 versus 0 (referring to δL_i)	–0.0587 h	–0.0016 h
a_D	Boundary above which dry stress is 1 versus 0 (referring to Q_i)	176.94	183.82
w_C	Weight of cold stress	0.14	0.29
w_P	Weight of photoperiod stress	0.02	0.52
w_D	Weight of dry stress	0.22	0.05
s_X	Scaling factor of the senescence rate	0.59	0.35
x_S	Shape parameter of the stress rate	0.21	5.67
$Y_{Aging,1}$	Age threshold for the transition from young to mature leaf	41.59 d	1.57 d
$Y_{Aging,2–Aging,1}$	The threshold of aging during the mature leaf phase	137.31 d	71.58 d
$Y_{Aging,2}$	Theoretical age threshold for the transition from mature to old leaf	178.90 d	73.14 d
Y_{LS100}	Senescence threshold for LS_{100} (all leaves have changed color or have fallen)	5.95	-

Note: The parameters refer to the equations 7 and 9–11 and were fitted for beech with the LS_{50} and LS_{50}-LS_{100} samples (Sect. 2.4). All parameters were calibrated within the initial ranges (Table S3) to their fitted value. To avoid fitted values of $Y_{Aging,1} > Y_{Aging,2}$, we used and calibrated $Y_{Aging,2–Aging,1}$ instead of $Y_{Aging,2}$. The theoretical threshold $Y_{Aging,2}$ was not calibrated but calculated from $Y_{Aging,1} + Y_{Aging,2–Aging,1}$ and displayed for easier interpretation. The thresholds for stress (Y_{Stress}) and LS_{50} (Y_{LS50}; i.e., the time when 50% of the leaves have changed color or have fallen) were hard coded with $Y_{Stress} = 1$ and $Y_{LS50} = 1$. The shortening of day length of 0.0016 h (a_P; ~~i.e.,~~corresponding to 0.1 minutes) based on the LS_{50} calibration is ~~b~~reached on doy 175, 174, and 174 (i.e., June 24, 23, and 23) at the exemplary minimum, median, and maximum latitudes of our samples (i.e., 45.9° N, 47.8° N, and 58.0° N ~~north~~), respectively. Alternatively, the shortening of 0.0587 h (3.5 minutes) based on the LS_{50}-LS_{100} calibration is ~~b~~reached on doy 252 and 202 (i.e., September 9 and July 21) at the ~~exemplary~~ median and maximum latitudes of our samples, respectively, whereas it is never ~~b~~reached at the ~~exemplary~~ minimum latitude.

According to the DP3 model, leaf senescence was generally induced earlier during warmer years and at lower elevations (Fig. 7; Tables S5–S8). In average, senescence was induced a month earlier when mean annual temperatures

370 were 13–15 °C than when they were 4–6 °C (i.e., May 29 versus June 22 and April 20 versus May 12 when the DP3 model was calibrated with the LS_{50}-LS_{100} and LS_{50} samples, respectively; hereafter referred to as 'DP3$_{LS_{50}-LS_{100}}$ model' and 'DP3$_{LS_{50}}$ model'; Sect. 2.4). Accordingly, senescence induction was 20 days earlier below 288 m a.s.l. than above 1150 m a.s.l. (i.e., June 5 versus June 25 and April 26 versus May 16 based on the DP3$_{LS_{50}-LS_{100}}$ and DP3$_{LS_{50}}$ model, respectively). Both the DP3$_{LS_{50}-LS_{100}}$ model and DP3$_{LS_{50}}$ model predicted generally longer-lasting senescence (i.e., the duration

375 between ~~LS_{50} or LS_{100} and~~ senescence induction and LS_{50} or LS_{100}) during years of higher mean annual temperatures (Fig. S3; Tables S5–S8).

Figure 7. Senescence induction. Panel (a) and (b) are based on simulations by the DP3 model calibrated with the LS_{50}-LS_{100} versus LS_{50} ~~versus LS50 LS100~~ samples, respectively (Sect. 2.4). The top row of each panel shows the number of site-years in the bins, which were equally distributed among mean annual temperature (MAT~~;~~; °C), mean annual Keetch and Byram drought index (MAQ), latitude (LAT~~;~~; °N), and elevation (ELV; m a.s.l.). The second row of each panel visualizes the ~~date of~~ senescence induction (SI) dates in day of year ~~[~~(doy)~~]~~. While the mean and median dates are marked with black dots and grey lines, respectively, the most extreme values are indicated with dots if outside ±1.5 times the inner quartile range from the 1st and 3rd quartile, and with whiskers otherwise. The third row of each panel illustrates the relative number of site-years during which senescence was induced by stress versus aging or by both stress and aging ~~[~~(i.e., both the accumulated stress ~~rate~~ and ~~accumulated~~ aging rate~~s~~ reached their thresholds for ~~senescence induction (SI~~) on the same date)~~]~~. The bottom row of each panel shows the relative amount~~s~~ of cold stress, photoperiod stress (Photop.), and dry stress that accumulated at ~~the time of senescence induction by~~ stress-caused SI.

Stress induced senescence two times and 40 times more often than aging according to the $DP3_{LS_{50}-LS_{100}}$ and $DP3_{LS_{50}}$ model, respectively (Fig. 7, Tables S5–S8). Thus, while aging was of negligible importance to senescence induction according to the $DP3_{LS_{50}}$ model, it mattered according to the $DP3_{LS_{50}-LS_{100}}$ model, particularly during years of medium mean annual temperature (6–13° C) as well as at sites of medium latitude (48.3–55.6 °N) and of low elevation (below 576 m a.s.l.). At the time of senescence induction due to stress, the amounts of accumulated photoperiod stress and cold stress relative to total stress were 56% versus 44% ($DP3_{LS_{50}-LS_{100}}$ model) and 77% versus 23% ($DP3_{LS_{50}}$ model), respectively, while the corresponding amounts of dry stress were 0.5% and 0.0%. Photoperiod stress dominated mostly in warm years and medium-elevation sites according to the $DP3_{LS_{50}-LS_{100}}$ model, whereas it did so in cool years and high-elevation sites according to the $DP3_{LS_{50}}$ model. In summary, photoperiod stress rather than cold and dry stress induced leaf senescence, but the importance of these stressors and their dependency on climatic conditions and location differed between the $DP3_{LS_{50}-LS_{100}}$ and $DP3_{LS_{50}}$ model.

Accordingly, the relative importance of these stressors for the duration of senescence differed between the $DP3_{LS_{50}-LS_{100}}$ and $DP3_{LS_{50}}$ model (Fig. S3; Tables S5–S8). Photoperiod stress clearly dominated the progress from senescence induction to LS_{50} according to the $DP3_{LS_{50}}$ model. However, according to the $DP3_{LS_{50}-LS_{100}}$ model and especially during cool years, cold stress was most important between senescence induction and LS_{50}, whereas photoperiod stress was most important between senescence induction and LS_{100}.

3.2 Model accuracy

Leaf senescence dates were predicted~~The DP3 model simulates leaf senescence~~ with similar accuracy by the DP3 model as ~~by~~ previous models (Fig. 8; Table 4). All models calibrated with the LS_{50} sample resulted in an RMSE of ~15 d, with the lowest RMSE for the Null model (i.e., constant prediction of each the average LS_{50} and LS_{100} observations in the calibration sample). The $LS_{50}-LS_{100}$ sample yielded considerable higher RMSE for both the $DP3_{LS_{50}-LS_{100}}$ and Null model, namely 23–25 d and 18–21 d, respectively. Nevertheless, the $DP3_{LS_{50}-LS_{100}}$ model resulted in the highest overall correlation ($\rho_{Overall}$ of 0.2 for LS_{100}). The highest correlation across space was obtained with the PIA model ($\rho_{Spatial}$ of 0.4), while the DP3 model resulted in the highest correlation across time (average $\rho_{Temproal}$ of 0.05 according to $DP3_{LS_{50}}$ and according to $DP3_{LS_{50}-LS_{100}}$ for LS_{100}).

Table 4. Model accuracy

Model	Sample	Stage	KGE'	RMSE	AICc	$\rho_{Overall}$	$\rho_{Spatial}$	$\overline{\rho}_{Temporal}$	n
CDD	LS_{50}	LS_{50}	-0.13	16.1	57797	0.01	-0.09	0.04	6887
DM2	LS_{50}	LS_{50}	-0.26	15.0	56862	0.02	-0.12	0.00	6887
PIA	LS_{50}	LS_{50}	-0.19	14.8	56701	0.10	0.44	-0.04	6887
$DP3_{LS_{50}}$	LS_{50}	LS_{50}	-0.23	15.2	57083	0.02	-0.02	0.05	6887
Null	LS_{50}	LS_{50}	NA	14.8	NA	NA	NA	NA	6887
$DP3_{LS_{50}-LS_{100}}$	$LS_{50}-LS_{100}$	LS_{50}	-0.01	25.0	63911	0.04	-0.06	0.03	6887
$DP3_{LS_{50}-LS_{100}}$	$LS_{50}-LS_{100}$	LS_{100}	0.14	23.2	NA	0.22	0.17	0.05	600
Null	$LS_{50}-LS_{100}$	LS_{50}	NA	18.1	NA	NA	NA	NA	6887
Null	$LS_{50}-LS_{100}$	LS_{100}	NA	21.7	NA	NA	NA	NA	600

Note: The Null model constantly predicts the average observation in the calibration sample (i.e., either the stage when 50% or 100% of the leaves have changed color or have fallen; LS_{50} or LS_{100}, respectively). The modified Kling-Gupta efficiency (KGE'), root mean squared error (RMSE), Akaike information criterion for small samples (AICc), and Pearson correlation overall, across space, and across time [$\rho_{Overall}$, $\rho_{Spatial}$, and average $\rho_{Temporal}$ ($\overline{\rho}_{Temporal}$), respectively] are explained in Sect. 2.6, S2.1, and S2.2. All these metrics were calculated for the ~~simulations~~predicted and observ~~ed dates in~~ations of the validation samples LS_{50} and $LS_{50}-LS_{100}$ (Sect. 2.4). Except the RMSE, they result in NA if the variance of the ~~simulated values~~predicted dates is zero, which is the case for the Null model. ~~n indicates the number of observations in the validation sample.~~ In addition, the AICc for the stage LS_{100} according to the model $DP3_{LS_{50}-LS_{100}}$ was omitted because n, i.e., the number of observations in the validation sample, differed between LS_{100} and LS_{50}.
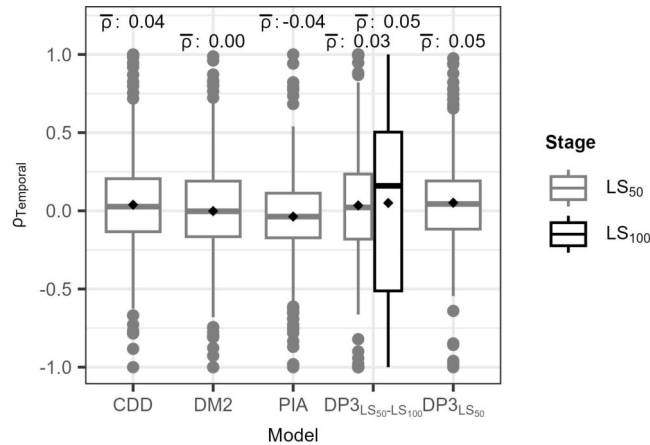
Figure 8. Temporal Pearson correlation ($\rho_{Temporal}$). The distribution ~~of the Pearson correlation within site~~of ($\rho_{Temporal}$) per site between ~~simulated~~predicted and observed leaf senescence [the dates when 50% and 100% of the leaves have changed color or have fallen (LS_{50} and LS_{100}, respectively)] is displayed for each model. The DP3 model was calibrated twice, namely with the LS_{50}-LS_{100} sample ($DP3_{LS_{50}-LS_{100}}$) and with the LS_{50} sample ($DP3_{LS_{50}}$; Sect. 2.4), the latter of which was also used to calibrate the CDD, DM2, and PIA model. The mean $\rho_{Temporal}$ (black rhombuses) is indicated above each box ($\bar{\rho}$). The boxes indicate the inner quartile range and the median (middle line). The most extreme values are indicated with dots if outside ±1.5 times the inner quartile range from the 1st and 3rd quartile, and with whiskers otherwise.

3.3 Model error

The model errors according to the DP3 model and previous models were similarly affected by data structure and climatic and spatial deviations from the calibration sample as the Null model (Fig. 9a). The data structure was described by the fixed effects of countries and the random intercepts grouped by sites. The countries altered the model error by –18 to +8 d, depending on the model (Tables S9–S10). The standard deviation in the model error due to the random intercepts was 9 d. Depending on the model, the fixed effects of the climatic deviations ranged from –22 to –19 d $10°C^{-1}$ (δMAT), from +3.6 to +9.0 d 100^{-1} (δMAQ), and from +4.1 to +4.6 d 10mol C^{-1} (δA_{net}), respectively. The model-specific effects of the spatial deviations δLAT and δELV ranged from +2.0 to +2.1 d $°N^{-1}$ and from +1.0 to +1.1 d $100m^{-1}$, respectively. While the evidence in the data was decisive ($\underline{BF}_{01} < 1/1000$; Sect. 2.7) and significant ($p < 0.005$) for an effect of the CDD model on the model error different from zero as well as for the individual climatic deviations and ~~for~~ δLAT, it was ~~. The evidence was~~ significant ~~($p < 0.005$)~~ for corresponding effects of the ~~CDD and~~ DM2 model as well as for δELV ~~all individual climatic and spatial deviations~~ and ~~for~~ all individual countries. The evidence was neither decisive nor significant for any effect different from zero of the interaction terms between the models and the climatic or spatial deviations. The LMM explained the model error with an adjusted R^2 of 0.44. Differences among sites attributed for 92% of the variance in the model error explained by the LMM, followed by the effects of δA_{net} and δMAT (6% and 2%, respectively), whereas the effects of the models accounted for 0.3% (Fig. 9b; Table S11). In general, the model errors according to the DP3 model and previous models behaved as those of the Null model and mainly varied due to data structure.
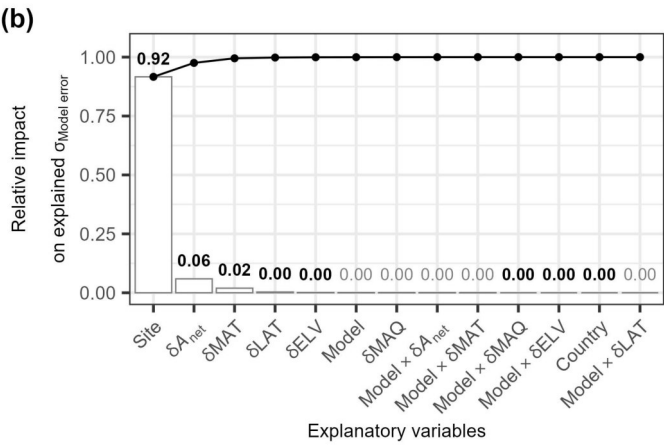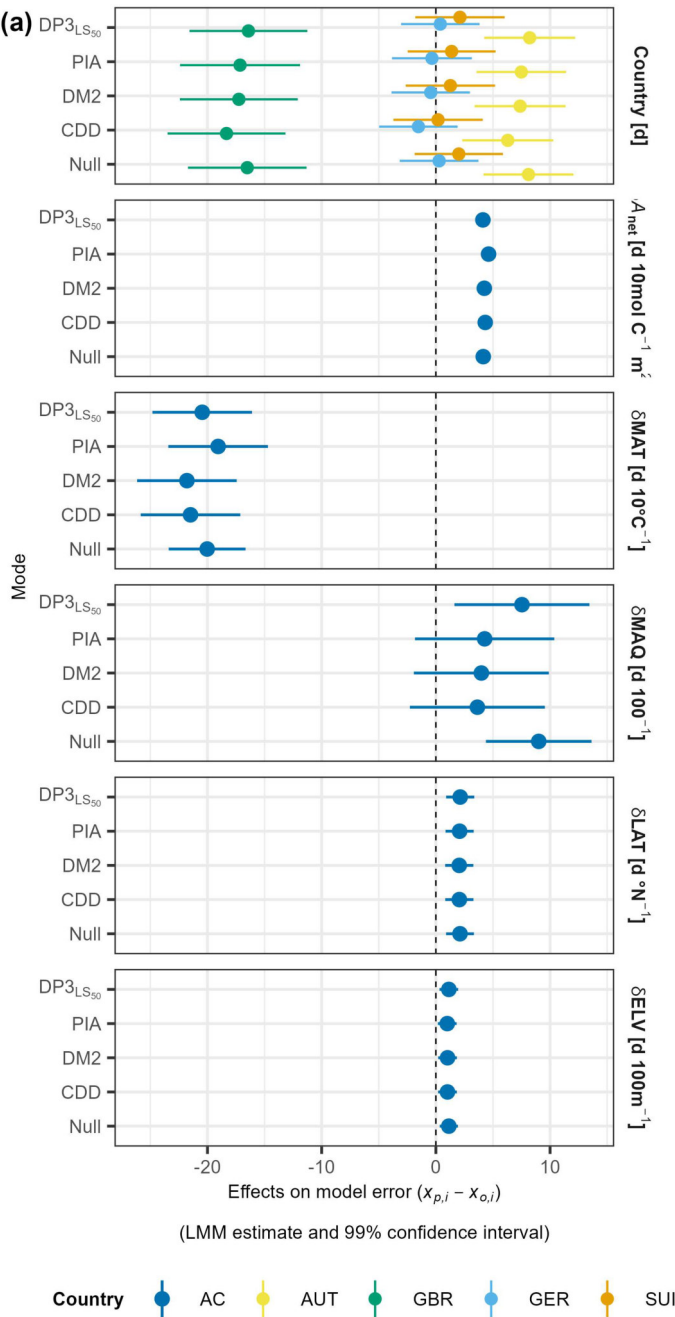
Earlier ~~start~~onset of leaf senescence in warmer years

(a)

Effects on model error ($x_{p,i} - x_{o,i}$)

(LMM estimate and 99% confidence interval)

Country: AC AUT GBR GER SUI

(b)

Figure 9. Model error versus data structure and climatic and spatial deviations. Panel (a) visualizes the LMM-based, model-specific estimated fixed effects (dots) and 99% confidence intervals (bars) of data structure described by 'country', climatic deviations described by mean annual temperature (δMAT; d 10°C^{-1}), mean annual Keetch and Byram drought index (δMAQ; d 100^{-1}), and accumulated net photosynthetic activity between leaf unfolding and summer solstice (δA_{net}; d 10mol C^{-1}), and spatial deviations described by latitude (δLAT; d °$\underline{N}^{-1}$) and elevation (δELV; d 100m^{-1}). These deviations were calculated as the difference between a given site-year and the average in the calibration sample. The colors indicate the countries Austria (AUT), Great Britain (GBR), Germany (GER), and Switzerland (SUI) as well as estimates across countries (AC). The model error was calculated as the ~~simulated~~predicted minus the observed timing ($x_{\sim p,i} - x_{o,i}$). Panel (b) shows, based on the ANOVA, the relative impact of the explanatory variables on the variance in the model error as explained by the LMM. The random intercepts in the LMM were grouped by 'site', also describing data structure. The bars indicate the impact of individual variables, while the connected dots show the accumulated impact. The numbers above each bar state the impact, being bold in case of combined significance and decisiveness (i.e., $p \leq 0.01$ and ~~minimum Bayes factor~~$BF_{01} \leq 1/1000$).

4   Discussion

4.1   Model formulation

The DP3 model ~~simulates~~predicts leaf senescence dates through a novel formulation that differs considerably from the formulation of current models. This novel formulation may change the way we see leaf senescence, namely as a consequence of leaf development that relates to both aging and stress. Current models start their simulation with the onset of senescence, i.e., ~~on~~ the senescence induction date, which they determine from day length and temperature (e.g., Delpierre et al., 2009; Dufrêne et al., 2005; Keenan and Richardson, 2015; Lang et al., 2019; Liu et al., 2019; Zani et al., 2020). This date is calibrated such that leaf senescence dates are ~~simulated~~predicted most accurately. In the DP3 model and in addition to this prerequisite, ~~at least~~ accumulated aging or accumulated stress since leaf unfolding must have reached a given threshold (i.e., $Y_{Aging,2}$ and Y_{Stress} as well as Figs. 3c and 3a, respectively; Table 3). In other words, while current models define the senescence induction date backward, the DP3 model defines it both backward and forward, arguably resulting in a more robust definition. Moreover, as current models generally ignore aging (but see the model by Keenan and Richardson, 2015, which considers the leaf unfolding date in the stress threshold for leaf senescence), their formulation partially ignores current knowledge (e.g., Field and Mooney, 1983; Guo et al., 2021; Jibran et al., 2013; Lim et al., 2007). In addition, the models by Liu et al. (2019) and Zani et al. (2020) postulate an effect of the conditions before senescence induction on senescence duration, which remains speculative. However, the~~se~~ conditions ~~before senescence induction~~ likely affect senescence induction dates, possibly through photosynthetic activity (Zohner et al., 2023) or through aging and stress (DP3 model).

The novel formulation of the DP3 model supports the advancement of leaf senescence research by postulating new hypotheses. To our knowledge, it is the first process-based leaf senescence model that (a) ~~simulates~~predicts leaf senescence dates through daily leaf development status, (b) starts the simulation with leaf unfolding, (c) differentiates between daily aging and stress rates, and (d) predicts the dates of transition between the leaf developmental phases young, mature, and old leaf as well as the ~~date of~~ senescence induction date. This allows the development of several new hypotheses (Carley, 1999; Hauke et al., 2020), which may relate to the currently disputed effect of climate change on productivity (Lu and Keenan, 2022; Norby, 2021; Zani et al., 2020; Zohner et al., 2023) and can be tested by controlled experiments. In particular, these hypotheses may concern (1) the duration of the young leaf phase during which stress cannot induce senescence, (2) the timing and cause (i.e., aging versus stress) of senescence induction, and (3) the

relative importance of the stressors in relationship to climate and location, all of which are further elaborated here below.

450   The duration of the young leaf phase differed considerably between the $DP3_{LS_{50}-LS_{100}}$ and $DP3_{LS_{50}}$ model (i.e., the DP3 models calibrated with the LS_{50}-LS_{100} versus LS_{50} samples; Sect. 2.4), namely 41 d versus 1 d, respectively. Because the DP3 assumes that stress during this phase is irrelevant for senescence induction, the duration of this phase affects the ~~date of the~~ induction and end of ~~leaf~~ senescence (see below). Moreover, corresponding projections under future climate scenarios are also likely affected, as the probability of late spring frost events likely will change under climate

455 warming (Bigler and Bugmann, 2018; Meier et al., 2018; Sangüesa-Barreda et al., 2021). Therefore, duration and characteristic of this young leaf phase should be examined further, e.g., with controlled experiments that apply continuous stress right after leaf unfolding to determine until when stress is either completely irrelevant for senescence induction or accumulates without inducing senescence.

    Senescence was induced in late spring/early summer and more often by stress than by aging, but the induc-

460 tion dates and the stress:aging ratios differed notably between the $DP3_{LS_{50}-LS_{100}}$ and $DP3_{LS_{50}}$ model. ~~The~~Senescence induction dates predicted by the $DP3_{LS_{50}-LS_{100}}$ and $DP3_{LS_{50}}$ models differed by 40 d, which matches the difference in the predicted duration of the young leaf phase (see above). As stress during the young leaf phase does not affect the predicted ~~timing of~~ leaf senescence dates by definition (Figs. 1, 3a, and 3c), this result illustrates the importance of studying the effects of stress after leaf unfolding (see above). It also shows that different combinations of calibrated model parame-

465 ters eventually yield similar predictions. Such compensating effects between different model parameters have also been reported in previous studies (Chuine and Régnière, 2017; Van der Meersch and Chuine, 2025), and explain the different stress:aging ratios as well as the earlier senescence induction during warmer years and at lower elevations. On the one hand, the ratio of stress to aging induced senescence shifts in favor of stress with shorter young leaf phases, because more cold stress can accumulate in spring. On the other hand, senescence must be induced earlier when senescence

470 lengthens to predict leaf senescence dates that are close to the average observation in the calibration sample, as suggested by model accuracy and model error (see below). Longer senescence, in turn, results from arguably reduced cold stress in fall in warmer years and at lower sites. Nevertheless, ~~In warmer years and at lower sites, cold stress arguably decreases more (see below) than dry stress increases, while photoperiod stress remains unaffected, which decelerates senescence. On the one hand, senescence must be induced earlier in warmer years and at lower sites to predict leaf~~

475 ~~senescence dates that are biased to the mean and constant, as suggested by model accuracy and model error (see below). On the other hand,~~ earlier induction and longer duration of senescence in warmer years may also be a valid description of reality (Yu et al., n.d.; Zohner et al., 2023). However, Zohner et al. (2023) argued that senescence induction dates relate negatively to pre-solstice productivity (see also Zani et al., 2020), whereas we showed that these dates relate to particular interactions between aging and stress rather than to productivity (see below; Eqs. 3 & 10; Lu and Keenan, 2022;

480 Marqués et al., 2023; Norby, 2021). Because such different mechanisms very likely affect leaf senescence projections under climate warming, they certainly need further investigations.

    How do aging and stress interact to predict earlier induction and longer duration of senescence in warmer years and at lower sites? The aging requirement for the transition from mature to old leaf (i.e., $Y_{Aging,2}$; Table 3) represents the longest possible duration from leaf unfolding to senescence induction. Earlier senescence induction is only

485 possible through sufficient stress between the transition from young to mature leaf and senescence induction (i.e., Y_{Stress}; Table 3), whereas stress after senescence induction, ~~which further~~ relates negatively to the duration of senescence. ~~At the same time, I~~Thus, according to the DP3 model, both earlier leaf unfolding and increased stress in spring advance

senescence induction, while reduced stress in summer and fall lengthens senescence, which corresponds to observed patterns. ~~L~~eaves unfold earlier at lower sites in general (Vitasse et al., 2009, 2013) and in warm springs in particular (given that the buds have been sufficiently chilled; Asse et al., 2018; Meier et al., 2021; Menzel et al., 2020). Warmer years have been shown to increase cold stress in spring (i.e., through leaves unfolding overly early in comparison to late frost; Asse et al., 2018; Meier et al., 2018; Sangüesa-Barreda et al., 2021) and relate positively to dry stress (i.e., through evapotranspiration; Allen et al., 1994; Berdanier and Clark, 2018; Wu et al., 2022), ~~while~~but leav~~ing~~ photoperiod stress unaffected (Brock, 1981). Thus, earlier senescence induction ~~results from~~is likely due to earlier leaf unfolding, and thus aging, and ~~in combination with~~ increased cold and dry stress in spring~~during the mature leaf phase~~, while the longer senescence duration ~~relates to decreased stress during senescence~~is likely due to the later accumulation of photoperiod stress relative to leaf development and reduced cold stress in summer and fall.

Surprisingly at first, the $DP3_{LS_{50}-LS_{100}}$ model postulated photoperiod rather than cold and dry stress of being the most important stressor for senescence induction during warmer years, whereas the $DP3_{LS_{50}}$ model saw photoperiod stress of being most important during cooler years. By definition, stress only ~~accumulates during the mature leaf phase but not during the young leaf phase~~matters when it occurs after the transition from young to mature leaf (Figs. 1, 3a, and 3c). ~~The threshold for p~~Photoperiod stress ~~is likely reached only during the mature leaf phase~~occurs, if at all, after this transition (i.e., after July 21 to September 9 in the $DP3_{LS_{50}-LS_{100}}$ model and after June 23–24 in the $DP3_{LS_{50}}$ model, depending on latitude; Table 3), and ~~unless senescence is induced soon after this day by either cold or dry stress, photoperiod stress~~ gains in importance quickly after the first occurrence unless senescence is induced soon by either cold or dry stress. ~~The threshold for c~~Cold stress ~~is~~likely ~~reached~~occurs in spring and ~~autumn~~fall, ~~and thus during~~ both ~~the young and mature leaf phases~~before and after the transition from young to mature leaf. Thus, cold days in spring are less likely to affect senescence induction the later the ~~longer the~~young leaf phase ~~and the later it~~ends, ~~the less likely late cold days in spring affect the senescence induction date~~ and vice versa. In addition, more cold days in fall can be accumulated the later ~~aging may induce senescence at the end of~~ the ~~young~~mature leaf phase ends and the later photoperiod stress starts to accumulate, ~~the more cold days in fall can be accumulated~~ and vice versa. Therefore, on the one hand, the long young leaf phase and late accumulation of photoperiod stress in the $DP3_{LS_{50}-LS_{100}}$ model favor the accumulation of cold stress in ~~autumn~~fall, which ~~likely~~arguably decreases in warmer years, making photoperiod stress relatively more important ~~in the $DP3_{LS_{50}-LS_{100}}$ model~~. On the other hand, the short young leaf phase in the $DP3_{LS_{50}}$ model favors the accumulation of cold stress in spring, which likely decreases in cooler years through leaves unfolding overly late in comparison to late frost (Asse et al., 2018; Meier et al., 2018; Sangüesa-Barreda et al., 2021), making photoperiod stress relatively more important ~~in the $DP3_{LS_{50}}$ model~~.

4.2   Model accuracy

We compared the DP3 model to three previous models of leaf senescence (i.e., the models CDD, DM2, and PIA; Delpierre et al., 2009; Dufrêne et al., 2005; Zani et al., 2020) based on the LS_{50} calibration sample and found the RMSE of all compared models to be above the RMSE for the Null model ~~(i.e. the constant prediction of the average observation in the calibration sample)~~. This may be explained by unrealistic model formulations, poor model calibrations, and noisy data to drive and calibrate the models, all of which we discuss here below.

While the formulations of the compared models differ, they all build on the results of previous studies. For example, according to all compared models, the leaf senescence date advances due to cold temperatures, which was also observed by Kloos et al. (2024), Wang et al. (2022), Wang and Liu (2023), and Xie et al. (2015, 2018). Moreover, in all

but one model, shorter days cause earlier leaf senescence, which is is in agreement with Addicott (1968), Keskitalo et al. (2005), Singh et al. (2017), Tan et al. (2023), and Wang et al. (2022). Therefore, while the Null model predicted the leaf senescence dates more accurately according to the RMSE, it is unlikely that it is more realistically formulated than the compared models. The currently most realistic model is arguably the DP3 model (Jan et al., 2019; Jibran et al., 2013; Lim et al., 2007), which makes it the first choice to study the leaf senescence process (see above). Moreover, while the Null model could be a good choice for predictions of leaf senescence dates (i.e., accuracy), the most suited models for predictions of leaf senescence trends (i.e., precision) may have to be identified yet.

We calibrated the compared models with the generalized simulated annealing algorithm and with model-specific controls (Sect. 2.4 and S2.1; Xiang et al., 1997, 2017). Algorithm and controls affect the accuracy of the calibrated models (Meier and Bigler, 2023). Therefore, we used generalized simulated annealing, which ~~is a well established optimization algorithm and~~ was shown to yield accurate models of leaf phenology (Chuine et al., 1998; Meier and Bigler, 2023) and has been used by many studies to calibrate such models (e.g., Basler, 2016; Liu et al., 2019; Meier et al., 2018; Zani et al., 2020). In addition, we used model-specific controls selected to most accurately ~~simulate~~predict leaf senescence dates for same the validation samples (Sect. S2.2) as the comparison to the Null model was based on. Possible overfitting (James et al., 2017) through this procedure would have benefited the compared models and is unlikely, as the number of observations in the calibration samples was large enough (Sect. 2.4; Jenkins and Quintana-Ascencio, 2020; Meier and Bigler, 2023). ~~Moreover, the compared models would have benefited from overfitting, as the comparison to the Null model was based on the same validation samples as the selection of the controls.~~ Therefore, it is highly improbable that this procedure caused the models to be calibrated so poorly that they are outperformed by the Null model.

All compared models were driven with daily weather data from the E-OBS dataset (Cornes et al., 2018) and calibrated and validated with leaf senescence data from the datasets of Meteo Swiss and PEP725 (Swiss phenology network, 2025; Templ et al., 2018). The E-OBS dataset has been used by many studies (e.g., Bowling et al., 2024; Meng et al., 2021; Schwaab et al., 2021; Zeng and Wolkovich, 2024), and we are unaware of any difficulties concerning the daily weather data used here. The Meteo Swiss and PEP725 datasets, however, compile visually observed leaf senescence data, and such data is noisy due to different observers and small sample sizes (Liu et al., 2021): estimates of the leaf senescence dates for individual trees varied by 15 d (median, spreading from 2–53 d) between observers, and increased to 28 d (median) for different samples of ten trees. The data become even noisier if the observers follow different protocols from various institutions and countries (Menzel, 2013), eventually blurring the signal of the leaf senescence process. Arguably the more this signal is blurred, the closer the simulations will follow the mean observation in the data. Here, we used leaf senescence data from 244 sites (i.e., probably at least 244 observers) and four countries (Sect. 2.1), which implies considerable noise and thus a blurred signal of the leaf development process. This data very likely forced the compared models to ~~simulate~~predict leaf senescence dates close to the mean observation, impairing their accuracy.

4.3   Model error

While ~~the model error was generally affected by~~ climatic and spatial deviations from the calibration sample generally affected the model error, their model-specific effects only differed insignificantly from the Null model. In other words, the model error in the compared models reacted similarly to climatic and spatial deviations as the model error of the Null model. This implies that the compared models ~~simulated~~predicted leaf senescence dates closely to the mean obser-

vation of the calibration sample and thus were heavily biased to the mean (i.e., as the Null model). Possible explanations for this are unrealistic model formulations, poor model calibrations, and noisy data. Interestingly, Meier et al. (2023), who reported a heavy bias towards the mean for 21 process-oriented models of leaf senescence, based their study on leaf senescence data from 500 sites (i.e., probably at least 500 observers) and at least three countries from the PEP725 dataset (Templ et al., 2018). This supports our inference that the compared models resorted to the mean observation due to the used leaf senescence data rather than to model formulations and model calibrations.

~~L~~Moreover, leaf senescence data was most relevant for the model error in the compared models, which was illustrated by the fixed effects of countries and the variation caused by the random intercepts grouped by sites. These effects of countries ~~have, to our knowledge, not been studied yet, and~~ differed considerably between countries, ~~which~~ demonstrat~~ing~~es ~~how~~~~the noise added to leaf senescence data by~~ different observation protocols (see above; Menzel, 2013)~~.~~ add noise to leaf senescence data, which to our knowledge has not yet been investigated. The random intercepts grouped by sites varied considerably, and corresponding differences among sites were attributed to a substantial amount of the explained variance in the model error (Chpt. 23.3.2 in Fox, 2016). Meier et al. (2023) also noted a large amount of the explained variance in the RMSE being attributed to differences among sites. They reasoned that this was caused by, among others, noisy leaf senescence data (see above) and different inter-annual variability of observations between the sites (Cole and Sheldon, 2017; Čufar et al., 2015; Li et al., 2022; Liu et al., 2020). It remains to be seen if such site-specific inter-annual variability as well as inter-site variability in leaf senescence dates would be ~~simulated~~predicted correctly by models calibrated with noise-free data.

4.4 Ways forward

While the DP3 model is likely the currently most realistic process-oriented model of leaf senescence, it may be developed further by (1) testing other drought indices, (2) considering nutrient depletion in combination with drought, and (3) ameliorating the formulation of the senescence rate. First, while various indices summarize drought differently (Speich, 2019; Zargar et al., 2011), the KBDI used here can be calculated from few data, being based on precipitation and temperature. It should be tested, however, if other indices, such as the standardized precipitation evapotranspiration index (based on precipitation and temperature; Vicente-Serrano et al., 2010) or the ratio of actual to potential evapotranspiration (based on precipitation, temperature, and soil moisture; Bugmann and Cramer, 1998), may approximate the effects of dry stress on leaf senescence more accurately. Second, despite more accurate ~~simulations~~predictions of LS_{50} and LS_{100} when nutrient depletion was disregarded (Figs. 6 and S1), model errors indicated earlier observed than ~~simulated~~predicted LS_{50} and LS_{100} dates due to nutrient depletion as approximated by elevation (Fig. 9; Tables S9–S10). This can be explained by higher elevation relating to increased nutrient depletion, which in turn fuels dry stress (Fu et al., 2014; Huber et al., 2007; Loomis et al., 2006; Tan et al., 2023). Consequently, drought indices that consider nutrient depletion should be tested. Third, the $DP3_{LS_{50}-LS_{100}}$ model was considerably less accurate than the $DP3_{LS_{50}}$ model, implying difficulties in the accurate ~~and,~~ simultaneous ~~simulation~~prediction of LS_{50} and LS_{100}. This points to an incorrectly formulated ~~curve~~dependency of the senescence rate on aging and stress (Eqs. 1 ~~&~~and 12), and corresponding new formulations should be evaluated.

In addition, because noisy data blur the signal of the leaf development process, (1) alternative data may be used, (2) observation protocols may be revised, and (3) visually observed data may be carefully selected. First, alternative data to calibrate and validate models of leaf senescence include data recorded with phenocams and remote sensed data in which leaf senescence dates are identified through the measured greenness, machine learning algorithms, and

610 vegetation indices (Donnelly et al., 2022; Dronova and Taddeo, 2022; Gong et al., 2024; Richardson, 2023; Zeng et al., 2020). While these data are species-specific if recorded with phenocams, this may not be the case for remote sensed data (Joiner et al., 2016; Tang et al., 2016). Second, revised observation protocols should describe how to determine dates of leaf senescence stages (i.e., senescence induction, LS_{50}, and LS_{100} at least) based on the measured, rather than estimated, state of leaf senescence. Such a measurement could be based on the greenness derived from images taken

615 with consumer-grade digital cameras (Ide and Oguma, 2013; Richardson et al., 2018; Toomey et al., 2015; Zimmerman and Richardson, 2024). Moreover, a given observational time series should be based on at least 25 trees which are measured every other week (Liu et al., 2021; Morellato et al., 2010). Third, visually observed leaf senescence data should be selected primarily from the point of view of precision, for example by ensuring identical observation protocols and by sampling from cleaned data with a minimum of breakpoints (i.e., sudden changes in the mean). For this, the time series

620 may be cleaned from outliers (Schaber et al., 2010) and separated ~~into series without sudden changes in the mean through a breakpoint analysis~~ (Auchmann et al., 2018), before being sampled, preferably through spatially and climatologically stratified sampling, according to the research focus (e.g., gaining insight in the underlying processes or producing most accurate or most precise predictions Meier and Bigler, 2023).

5   Conclusion

The DP3 model builds on three subsequent phases of leaf development: the young, mature, and old leaf phase. The
625 young leaf is insensitive to stress and transfers into a mature leaf solely due to aging. The mature leaf answers to aging and stress, both of which may induce senescence. While aging induces senescence with the transition from mature to old leaf, stress may already ~~do~~es so during the mature leaf phase through combining cold stress, photoperiod stress, and dry stress. The output of the DP3 model includes daily rates of aging rates as well as of cold, photoperiod, and dry stress along with the dates of transition from young to mature to old leaf, senescence induction dates, and the leaf senescence
630 dates. Thus, the DP3 model allows to develop testable hypotheses about the leaf senescence process, for example regarding the effect of site conditions on the ~~timing of senescence~~ induction and ~~the~~ duration of senescence ~~as well as on the relative importance of cold, photoperiod, and dry stress. For example,:~~ the DP3 model predicted earlier onset of senescence (i.e., senescence induction) ~~for~~under warmer conditions, likely due to earlier leaf unfolding and thus aging, and increased cold and drought stress in spring, as well as ~~and together with~~ longer-lasting senescence, likely due to the
635 later accumulation of photoperiod stress relative to leaf development and reduced cold stress in summer and fall. Both these predictions and their implied relationships with aging and stress can, ~~which may~~ be tested through experiments and in situ observations. This makes the DP3 model an important tool in the research of leaf senescence.

The accuracy of the DP3 model and of previous models of leaf senescence was lower than the accuracy of the Null model (i.e. the constant prediction of the average observation in the calibration sample). This was probably due
640 to model formulations that do not fully reflect the leaf senescence process and, more importantly, to the leaf senescence data used for calibration and validation. Visually observed leaf senescence data are susceptible to observer bias and based on observation protocols that are partly inconsistent between countries. Such noisy data blur the signal of the leaf senescence process, thereby probably forcing the models to resort to the average observation. This leads to low accuracy, regardless from the model formulation, which hinders the necessary further development of process-oriented mod-
645 els of leaf senescence.

The model error of the compared models was similarly affected by climatic and spatial deviations from the calibration sample across models, and varied mainly due to the leaf senescence data. The similar effect of climatic and

spatial deviations on the model error across models (including the Null model) illustrates that these models were heavily biased towards the mean. Moreover, the degree of noise in the used leaf senescence data is exemplified by these data accounting for over 90% of the explained variance in the model error. Therefore, these data should be selected with particular attention to precision, e.g., by using ~~as few sites with identical observation protocols as possible~~time series without sudden changes in the mean. Moreover, revised observation protocols should include senescence induction dates and rely on measurements rather than visual estimates. Such measurements may be based on the greenness of leaves to identify the degree of color change, involving digital cameras and automated image assessment.

Code and data availability

The R code for the DP3 model is openly available on Zenodo (Meier, 2025b, https://doi.org/10.5281/zenodo.14749339), together with the R code for the 2-phased version of the DP3 model ('DP2 model'), i.e., the DP3 model without young leaf phase. While all raw data used are publicly available and referenced in section 2, the ~~simulated~~predicted leaf senescence ~~data~~dates analyzed and compared ~~are~~is openly accessible under https://doi.org/10.5061/dryad.tht76hf97 (Meier, 2025a).

Author contributions

MM, IC, and CB initialized the study and the model development~~. MM and IC conceptualized~~, while the final study and model development were conceptualized MM and IC. MM designed the methodology and created the models, analyzed the models with input from IC and CB, visualized the results with input from IC, and wrote the draft with contributions from IC and CB. All authors approved the final manuscript.

Competing interests

The authors declare that they have no conflict of interest.

Acknowledgments

References

Addicott, F. T.: Environmental factors in the physiology of abscission, Plant Physiol., 43, 1471–9, https://doi.org/PMID: 16657013, PMCID: PMC1087141., 1968.

Akaike, H.: A new look at the statistical model identification, IEEE Trans. Autom. Control, 19, 716–723, https://doi.org/10.1109/TAC.1974.1100705, 1974.

Allen, R. G., Smith, M., Perrier, A., and Pereira, L. S.: An update for the definition of reference evapotranspiration, ICID Bull., 43, 1–34, 1994.

Asse, D., Chuine, I., Vitasse, Y., Yoccoz, N. G., Delpierre, N., Badeau, V., Delestrade, A., and Randin, C. F.: Warmer winters reduce the advance of tree spring phenology induced by warmer springs in the Alps, Agric. For. Meteorol., 252, 220–230, https://doi.org/10.1016/j.agrformet.2018.01.030, 2018.

Auchmann, R., Brugnara, Y., Brönnimann, S., Gehrig, R., Pietragalla, B., Begert, M., Sigg, C., Knechtl, V., Calpini, B., and Konzelmann, T.: Quality Analysis and Classification of Data Series from the Swiss Phenology Network, MeteoSwiss, Zürich-Flughafen, 2018.

Barrett, T., Dowle, M., Srinivasan, A., Gorecki, J., Chirico, M., and Hocking, T.: data.table: Extension of `data.frame`, 2024.

Basler, D.: Evaluating phenological models for the prediction of leaf-out dates in six temperate tree species across central Europe, Agric. For. Meteorol., 217, 10–21, https://doi.org/10.1016/j.agrformet.2015.11.007, 2016.

Berdanier, A. B. and Clark, J. S.: Tree water balance drives temperate forest responses to drought, Ecology, 99, 2506–2514, https://doi.org/10.1002/ecy.2499, 2018.

Bigler, C. and Bugmann, H.: Climate-induced shifts in leaf unfolding and frost risk of European trees and shrubs, Sci Rep, 8, 9865, https://doi.org/10.1038/s41598-018-27893-1, 2018.

Bigler, C. and Vitasse, Y.: Premature leaf discoloration of European deciduous trees is caused by drought and heat in late spring and cold spells in early fall, Agric. For. Meteorol., 307, 108492, https://doi.org/10.1016/j.agrformet.2021.108492, 2021.

Bivand, R. S., Pebesma, E., and Gomez-Rubio, V.: Applied spatial data analysis with R, Second edition., Springer, New York, USA, 2013.

Bowling, D. R., Schädel, C., Smith, K. R., Richardson, A. D., Bahn, M., Arain, M. A., Varlagin, A., Ouimette, A. P., Frank, J. M., Barr, A. G., Mammarella, I., Šigut, L., Foord, V., Burns, S. P., Montagnani, L., Litvak, M. E., Munger, J. W., Ikawa, H., Hollinger, D. Y., Blanken, P. D., Ueyama, M., Matteucci, G., Bernhofer, C., Bohrer, G., Iwata, H., Ibrom, A., Pilegaard, K., Spittlehouse, D. L., Kobayashi, H., Desai, A. R., Staebler, R. M., and Black, T. A.: Phenology of Photosynthesis in Winter-Dormant Temperate and Boreal Forests: Long-Term Observations From Flux Towers and Quantitative Evaluation of Phenology Models, J. Geophys. Res. Biogeosciences, 129, e2023JG007839, https://doi.org/10.1029/2023JG007839, 2024.

Brock, T. D.: Calculating solar radiation for ecological studies, Ecol. Model., 14, 1–19, https://doi.org/10.1016/0304-3800(81)90011-9, 1981.

Bugmann, H. and Cramer, W.: Improving the behaviour of forest gap models along drought gradients, For. Ecol. Manag., 103, 247–263, https://doi.org/10.1016/s0378-1127(97)00217-x, 1998.

Burnham, K. P. and Anderson, D. R.: Multimodel Inference: Understanding AIC and BIC in Model Selection, Sociol. Methods Res., 33, 261–304, https://doi.org/10.1177/0049124104268644, 2004.

Carley, K. M.: On generating hypotheses using computer simulations, Syst. Eng., 2, 69–77, https://doi.org/10.1002/(SICI)1520-6858(1999)2:2<69::AID-SYS3>3.0.CO;2-0, 1999.

Cheng, W., Dan, L., Deng, X., Feng, J., Wang, Y., Peng, J., Tian, J., Qi, W., Liu, Z., Zheng, X., Zhou, D., Jiang, S., Zhao, H., and Wang, X.: Global monthly gridded atmospheric carbon dioxide concentrations under the historical and future scenarios, Sci. Data, 9, 83, https://doi.org/10.1038/s41597-022-01196-7, 2022.

Chuine, I. and Régnière, J.: Process-based models of phenology for plants and animals, Annu. Rev. Ecol. Evol. Syst., 48, 159–182, https://doi.org/10.1146/annurev-ecolsys-110316-022706, 2017.

Chuine, I., Cour, P., and Rousseau, D. D.: Fitting models predicting dates of flowering of temperate-zone trees using simulated annealing, Plant Cell Environ., 21, 455–466, https://doi.org/10.1046/j.1365-3040.1998.00299.x, 1998.

Chuine, I., de Cortazar-Atauri, I. G., Kramer, K., and Hänninen, H.: Plant development models, in: Phenology: An integrative environmental science, edited by: Schwartz, M. D., Springer Netherlands, Dordrecht, 275–293, 2013.

Cole, E. F. and Sheldon, B. C.: The shifting phenological landscape: Within- and between-species variation in leaf emergence in a mixed-deciduous woodland, Ecol. Evol., 7, 1135–1147, https://doi.org/10.1002/ece3.2718, 2017.

Collatz, G. J., Ball, J. T., Grivet, C., and Berry, J. A.: Physiological and environmental-regulation of stomatal conductance, photosynthesis and transpiration - A model that includes laminar boundary-layer, Agric. For. Meteorol., 54, 107–136, https://doi.org/10.1016/0168-1923(91)90002-8, 1991.

Cooke, J. E. K. and Weih, M.: Nitrogen storage and seasonal nitrogen cycling in Populus: bridging molecular physiology and ecophysiology, New Phytol., 167, 19–30, https://doi.org/10.1111/j.1469-8137.2005.01451.x, 2005.

Copernicus Climate Change Service, Climate Data Store: Carbon dioxide data from 2002 to present derived from satellite observations. Copernicus Climate Change Service (C3S) Climate Data Store (CDS), last access: 30 April 2024, https://doi.org/10.24381/cds.f74805c8, 2018.

Copernicus Climate Change Service, Climate Data Store: E-OBS daily gridded meteorological data for Europe from 1950 to present derived from in-situ observations. Copernicus Climate Change Service (C3S) Climate Data Store (CDS), last access: 10 June 2023, https://doi.org/10.24381/cds.151d3ec6, 2020.

Cornes, R. C., van der Schrier, G., van den Besselaar, E. J. M., and Jones, P. D.: An Ensemble Version of the E-OBS Temperature and Precipitation Data Sets, J. Geophys. Res. Atmospheres, 123, 9391–9409, https://doi.org/10.1029/2017JD028200, 2018.

Čufar, K., De Luis, M., Prislan, P., Gricar, J., Crepinsek, Z., Merela, M., and Kajfez-Bogataj, L.: Do variations in leaf phenology affect radial growth variations in Fagus sylvatica?, Int J Biometeorol, 59, 1127–1132, https://doi.org/10.1007/s00484-014-0896-3, 2015.

Delpierre, N., Dufrene, E., Soudani, K., Ulrich, E., Cecchini, S., Boe, J., and Francois, C.: Modelling interannual and spatial variability of leaf senescence for three deciduous tree species in France, Agric. For. Meteorol., 149, 938–948, https://doi.org/10.1016/j.agrformet.2008.11.014, 2009.

Donnelly, A., Yu, R., Jones, K., Belitz, M., Li, B., Duffy, K., Zhang, X., Wang, J., Seyednasrollah, B., Gerst, K. L., Li, D., Kaddoura, Y., Zhu, K., Morisette, J., Ramey, C., and Smith, K.: Exploring discrepancies between in situ phenology and remotely derived phenometrics at NEON sites, Ecosphere, 13, e3912, https://doi.org/10.1002/ecs2.3912, 2022.

Dronova, I. and Taddeo, S.: Remote sensing of phenology: Towards the comprehensive indicators of plant community dynamics from species to regional scales, J. Ecol., 110, 1460–1484, https://doi.org/10.1111/1365-2745.13897, 2022.

Dufrêne, E., Davi, H., Francois, C., le Maire, G., Le Dantec, V., and Granier, A.: Modelling carbon and water cycles in a beech forest: Part I: Model description and uncertainty analysis on modelled NEE, Ecol. Model., 185, 407–436, https://doi.org/10.1016/j.ecolmodel.2005.01.004, 2005.

Dunnington, D.: ggspatial: Spatial data framework for ggplot2, 2023.

PEP725: http://www.pep725.eu/, last access: 25 June 2024.

EU-DEM: https://ec.europa.eu/eurostat/web/gisco/geodata/digital-elevation-model/eu-dem, last access: 25 July 2024.

Farquhar, G. D., von Caemmerer, S., and Berry, J. A.: A biochemical model of photosynthetic CO_2 assimilation in leaves of C3 species, Planta, 149, 78–90, https://doi.org/10.1007/bf00386231, 1980.

Field, C. and Mooney, H. A.: Leaf age and seasonal effects on light, water, and nitrogen use efficiency in a California shrub, Oecologia, 56, 348–355, https://doi.org/10.1007/BF00379711, 1983.

Fox, J.: Applied regression analysis and generalized linear models, 3rd ed., Sage Publications, Thousand Oaks, California, USA, 2016.

Fox, J. and Weisberg, S.: An R Companion to Applied Regression, Third., SAGE, Los Angeles, 2019.

Fu, Y. H., Campioli, M., Vitasse, Y., De Boeck, H. J., Van den Berge, J., AbdElgawad, H., Asard, H., Piao, S. L., Deckmyn, G., and Janssens, I. A.: Variation in leaf flushing date influences autumnal senescence and next year's flushing date in two temperate tree species, Proc. Natl. Acad. Sci. U. S. A., 111, 7355–7360, https://doi.org/10.1073/pnas.1321727111, 2014.

Fu, Y. H., Piao, S. L., Delpierre, N., Hao, F. H., Hanninen, H., Geng, X. J., Penuelas, J., Zhang, X., Janssens, I. A., and Campioli, M.: Nutrient availability alters the correlation between spring leaf-out and autumn leaf senescence dates, Tree Physiol., 39, 1277–1284, https://doi.org/10.1093/treephys/tpz041, 2019.

Gong, Z., Ge, W., Guo, J., and Liu, J.: Satellite remote sensing of vegetation phenology: Progress, challenges, and opportunities, ISPRS J. Photogramm. Remote Sens., 217, 149–164, https://doi.org/10.1016/j.isprsjprs.2024.08.011, 2024.

Grolemund, G. and Wickham, H.: Dates and Times Made Easy with lubridate, J. Stat. Softw., 40, 1–25, https://doi.org/10.18637/jss.v040.i03, 2011.

Guo, Y., Ren, G., Zhang, K., Li, Z., Miao, Y., and Guo, H.: Leaf senescence: progression, regulation, and application, Mol. Hortic., 1, 5, https://doi.org/10.1186/s43897-021-00006-9, 2021.

Gupta, H. V., Kling, H., Yilmaz, K. K., and Martinez, G. F.: Decomposition of the mean squared error and NSE performance criteria: Implications for improving hydrological modelling, J. Hydrol., 377, 80–91, https://doi.org/10.1016/j.jhydrol.2009.08.003, 2009.

Hauke, J., Achter, S., and Meyer, M.: Theory Development Via Replicated Simulations and the Added Value of Standards, J. Artif. Soc. Soc. Simul., 23, 12, https://doi.org/10.18564/jasss.4219, 2020.

Held, L. and Ott, M.: On p-Values and Bayes Factors, Annu. Rev. Stat. Its Appl., 5, 393–419, https://doi.org/10.1146/annurev-statistics-031017-100307, 2018.

Helwig, N. E.: npreg: Nonparametric Regression via Smoothing Splines, 2024.

Herms, D. A. and Mattson, W. J.: The dilemma of plants - To grow or defend, Q. Rev. Biol., 67, 283–335, https://doi.org/10.1086/417659, 1992.

Hijmans, R. J.: raster: Geographic Data Analysis and Modeling, 2023.

Huber, E., Wanek, W., Gottfried, M., Pauli, H., Schweiger, P., Arndt, S. K., Reiter, K., and Richter, A.: Shift in soil–plant nitrogen dynamics of an alpine–nival ecotone, Plant Soil, 301, 65–76, https://doi.org/10.1007/s11104-007-9422-2, 2007.

Ide, R. and Oguma, H.: A cost-effective monitoring method using digital time-lapse cameras for detecting temporal and spatial variations of snowmelt and vegetation phenology in alpine ecosystems, Ecol. Inform., 16, 25–34, https://doi.org/10.1016/j.ecoinf.2013.04.003, 2013.

James, G., Witten, D., Hastie, T., and Tibishirani, R.: An introduction to statistical learning: with applications in R, Springer, New York a.o., 2017.

Jan, S., Abbas, N., Ashraf, M., and Ahmad, P.: Roles of potential plant hormones and transcription factors in controlling leaf senescence and drought tolerance, Protoplasma, 256, 313–329, https://doi.org/10.1007/s00709-018-1310-5, 2019.

Jenkins, D. G. and Quintana-Ascencio, P. F.: A solution to minimum sample size for regressions, PLoS One, 15, e0229345, https://doi.org/10.1371/journal.pone.0229345, 2020.

Jibran, R., Hunter, D. A., and Dijkwel, P. P.: Hormonal regulation of leaf senescence through integration of developmental and stress signals, Plant Mol. Biol., 82, 547–561, https://doi.org/10.1007/s11103-013-0043-2, 2013.

Johnson, V. E.: Bayes Factors based on test statistics, J. R. Stat. Soc. Ser. B Stat. Methodol., 67, 689–701, 2005.

Joiner, J., Yoshida, Y., Guanter, L., and Middleton, E. M.: New methods for the retrieval of chlorophyll red fluorescence from hyperspectral satellite instruments: simulations and application to GOME-2 and SCIAMACHY, Atmospheric Meas. Tech., 9, 3939–3967, https://doi.org/10.5194/amt-9-3939-2016, 2016.

Kassambara, A.: ggpubr: "ggplot2" Based Publication Ready Plots, 2020.

Keenan, T. F. and Richardson, A. D.: The timing of autumn senescence is affected by the timing of spring phenology: implications for predictive models, Glob Chang Biol, 21, 2634–2641, https://doi.org/10.1111/gcb.12890, 2015.

Keetch, J. J. and Byram, G. M.: A Drought Index for Forest Fire Control, Department of Agriculture, Forest Service, Southeastern Forest Experiment Station, Asheville, NC: U.S., 1968.

Keskitalo, J., Bergquist, G., Gardestrom, P., and Jansson, S.: A cellular timetable of autumn senescence, Plant Physiol., 139, 1635–1648, https://doi.org/10.1104/pp.105.066845, 2005.

Kling, H., Fuchs, M., and Paulin, M.: Runoff conditions in the upper Danube basin under an ensemble of climate change scenarios, J. Hydrol., 424–425, 264–277, https://doi.org/10.1016/j.jhydrol.2012.01.011, 2012.

Kloos, S., Klosterhalfen, A., Knohl, A., and Menzel, A.: Decoding autumn phenology: Unraveling the link between observation methods and detected environmental cues, Glob. Change Biol., 30, e17231, https://doi.org/10.1111/gcb.17231, 2024.

Lang, W., Chen, X., Qian, S., Liu, G., and Piao, S.: A new process-based model for predicting autumn phenology: How is leaf senescence controlled by photoperiod and temperature coupling?, Agric. For. Meteorol., 268, 124–135, https://doi.org/10.1016/j.agrformet.2019.01.006, 2019.

Li, S., Wang, Y., Ciais, P., Sitch, S., Sato, H., Shen, M., Chen, X., Ito, A., Wu, C., Kucharik, C. J., and Yuan, W.: Deficiencies of Phenology Models in Simulating Spatial and Temporal Variations in Temperate Spring Leaf Phenology, J. Geophys. Res. Biogeosciences, 127, e2021JG006421, https://doi.org/10.1029/2021JG006421, 2022.

Lim, P. O., Kim, H. J., and Gil Nam, H.: Leaf senescence, Annu. Rev. Plant Biol., 58, 115–136, https://doi.org/10.1146/annurev.arplant.57.032905.105316, 2007.

Liu, G., Chen, X. Q., Zhang, Q. H., Lang, W. G., and Delpierre, N.: Antagonistic effects of growing season and autumn temperatures on the timing of leaf coloration in winter deciduous trees, Glob. Change Biol., 24, 3537–3545, https://doi.org/10.1111/gcb.14095, 2018.

Liu, G., Chen, X. Q., Fu, Y. S., and Delpierre, N.: Modelling leaf coloration dates over temperate China by considering effects of leafy season climate, Ecol. Model., 394, 34–43, https://doi.org/10.1016/j.ecolmodel.2018.12.020, 2019.

Liu, G., Chuine, I., Denechere, R., Jean, F., Dufrene, E., Vincent, G., Berveiller, D., and Delpierre, N.: Higher sample sizes and observer inter-calibration are needed for reliable scoring of leaf phenology in trees, J. Ecol., 109, 2461–2474, https://doi.org/10.1111/1365-2745.13656, 2021.

Liu, Q., Piao, S. L., Campioli, M., Gao, M. D., Fu, Y. S. H., Wang, K., He, Y., Li, X. Y., and Janssens, I. A.: Modeling leaf senescence of deciduous tree species in Europe, Glob. Change Biol., 26, 4104–4118, https://doi.org/10.1111/gcb.15132, 2020.

Loomis, P. F., Ruess, R. W., Sveinbjörnsson, B., and Kielland, K.: Nitrogen cycling at treeline: Latitudinal and elevational patterns across a boreal landscape, Ecoscience, 13, 544–556, https://doi.org/10.2980/1195-6860(2006)13[544:NCATLA]2.0.CO;2, 2006.

Lu, X. and Keenan, T. F.: No evidence for a negative effect of growing season photosynthesis on leaf senescence timing, Glob. Change Biol., 28, 3083–3093, https://doi.org/10.1111/gcb.16104, 2022.

Luo, Y.: Terrestrial carbon-cycle feedback to climate warming, Annu. Rev. Ecol. Evol. Syst., 38, 683–712, https://doi.org/10.1146/annurev.ecolsys.38.091206.095808, 2007.

Mao, J. and Yan, B.: Global monthly mean leaf area index climatology, 1981-2015 (1), https://doi.org/10.3334/ORNLDAAC/1653, 2019.

Mariën, B., Dox, I., De Boeck, H. J., Willems, P., Leys, S., Papadimitriou, D., and Campioli, M.: Does drought advance the onset of autumn leaf senescence in temperate deciduous forest trees?, Biogeosciences, 18, 3309–3330, https://doi.org/10.5194/bg-18-3309-2021, 2021.

Marqués, L., Hufkens, K., Bigler, C., Crowther, T. W., Zohner, C. M., and Stocker, B. D.: Acclimation of phenology relieves leaf longevity constraints in deciduous forests, Nat. Ecol. Evol., 7, 198–204, https://doi.org/10.1038/s41559-022-01946-1, 2023.

Massicotte, P. and South, A.: rnaturalearth: World Map Data from Natural Earth, 2023.

Meier, M.: Simulated and observed timings of leaf senescence for Fagus sylvatica (L.) at selected European sites, https://doi.org/10.5061/dryad.tht76hf97, 2025a.

Meier, M.: The DP3 model (v1.1) - Simulating the timing of leaf senescence, , Zenodo, https://doi.org/10.5281/zenodo.14749339, 2025b.

Meier, M. and Bigler, C.: Process-oriented models of autumn leaf phenology: ways to sound calibration and implications of uncertain projections, Geosci. Model Dev., 16, 7171–7201, https://doi.org/10.5194/gmd-16-7171-2023, 2023.

Meier, M., Fuhrer, J., and Holzkaemper, A.: Changing risk of spring frost damage in grapevines due to climate change? A case study in the Swiss Rhone Valley, Int. J. Biometeorol., 62, 991–1002, https://doi.org/10.1007/s00484-018-1501-y, 2018.

Meier, M., Vitasse, Y., Bugmann, H., and Bigler, C.: Phenological shifts induced by climate change amplify drought for broad-leaved trees at low elevations in Switzerland, Agric. For. Meteorol., 307, 108485, https://doi.org/10.1016/j.agrformet.2021.108485, 2021.

Meier, M., Bugmann, H., and Bigler, C.: Process-oriented models of leaf senescence are biased towards the mean: Impacts on model performance and future projections, Glob. Change Biol., 30, https://doi.org/10.1111/gcb.17099, 2023.

Meier, U.: Growth stages of mono- and dicotyledonous plants: BBCH Monograph, Open Agrar Repositorium, Quedlinburg, 2018.

Meng, L., Zhou, Y. Y., Gu, L. H., Richardson, A. D., Penuelas, J., Fu, Y. S., Wang, Y. Q., Asrar, G. R., De Boeck, H. J., Mao, J. F., Zhang, Y. G., and Wang, Z. S.: Photoperiod decelerates the advance of spring phenology of six deciduous tree species under climate warming, Glob. Change Biol., 27, 2914–2927, https://doi.org/10.1111/gcb.15575, 2021.

Menzel, A.: Europe, in: Phenology: An Integrative Environmental Science, edited by: Schwartz, M. D., Springer Netherlands, Dordrecht, 53–65, https://doi.org/10.1007/978-94-007-6925-0_4, 2013.

Menzel, A., Yuan, Y., Matiu, M., Sparks, T., Scheifinger, H., Gehrig, R., and Estrella, N.: Climate change fingerprints in recent European plant phenology, Glob. Change Biol., 26, 14, https://doi.org/10.1111/gcb.15000, 2020.

Swiss phenology network: https://www.meteoswiss.admin.ch/weather/measurement-systems/land-based-stations/swiss-phenology-network.html, last access: 29 January 2025.

Morellato, L. P. C., Camargo, M. G. G., D'Eça Neves, F. F., Luize, B. G., Mantovani, A., and Hudson, I. L.: The Influence of Sampling Method, Sample Size, and Frequency of Observations on Plant Phenological Patterns and Interpretation in Tropical Forest Trees, in: Phenological Research: Methods for Environmental and Climate Change Analysis, edited by: Hudson, I. L. and Keatley, M. R., Springer Netherlands, Dordrecht, 99–121, 2010.

Norby, R. J.: Comment on "Increased growing-season productivity drives earlier autumn leaf senescence in temperate trees," Science, 371, eabg1438, https://doi.org/10.1126/science.abg1438, 2021.

Paul, M. J. and Foyer, C. H.: Sink regulation of photosynthesis, J. Exp. Bot., 52, 1383–1400, https://doi.org/10.1093/jexbot/52.360.1383, 2001.

Pebesma, E.: Simple features for R: Standardized support for spatial vector data, R J., 10, 439–446, https://doi.org/10.32614/RJ-2018-009, 2018.

Pebesma, E. and Bivand, R. S.: Classes and methods for spatial data in R, R News, 5, 9–13, 2005.

Pebesma, E. and Bivand, R. S.: Spatial Data Science: With Applications in R, Chapman HallCRC, https://doi.org/10.1201/9780429459016, 2023.

Piao, S. L., Liu, Q., Chen, A. P., Janssens, I. A., Fu, Y. S., Dai, J. H., Liu, L. L., Lian, X., Shen, M. G., and Zhu, X. L.: Plant phenology and global climate change: Current progresses and challenges, Glob. Change Biol., 25, 1922–1940, https://doi.org/10.1111/gcb.14619, 2019.

Pierce, D.: ncdf4: Interface to Unidata netCDF (Version 4 or Earlier) Format Data Files, 2023.

Pinheiro, J. C. and Bates, D. M.: Mixed-effects models in S and S-PLUS, Springer, New York, 528 S. pp., 2000.

R Core Team: R: A language and environment for statistical computing, 2025.

Richardson, A. D.: PhenoCam: An evolving, open-source tool to study the temporal and spatial variability of ecosystem-scale phenology, Agric. For. Meteorol., 342, 109751, https://doi.org/10.1016/j.agrformet.2023.109751, 2023.

Richardson, A. D., Keenan, T. F., Migliavacca, M., Ryu, Y., Sonnentag, O., and Toomey, M.: Climate change, phenology, and phenological control of vegetation feedbacks to the climate system, Agric. For. Meteorol., 169, 156–173, https://doi.org/10.1016/j.agrformet.2012.09.012, 2013.

Richardson, A. D., Hufkens, K., Milliman, T., Aubrecht, D. M., Chen, M., Gray, J. M., Johnston, M. R., Keenan, T. F., Klosterman, S. T., Kosmala, M., Melaas, E. K., Friedl, M. A., and Frolking, S.: Tracking vegetation phenology across diverse North American biomes using PhenoCam imagery, Sci. Data, 5, 24, https://doi.org/10.1038/sdata.2018.28, 2018.

Rogers, H. J.: Leaf senescence, in: Encyclopedia of Applied Plant Sciences (Second Edition), vol. 1, edited by: Thomas, B., Murray, B. G., and Murphy, D. J., Academic Press, Amsterdam, 308–314, 2017.

Sangüesa-Barreda, G., Di Filippo, A., Piovesan, G., Rozas, V., Di Fiore, L., García-Hidalgo, M., García-Cervigón, A. I., Muñoz-Garachana, D., Baliva, M., and Olano, J. M.: Warmer springs have increased the frequency and extension of late-frost defoliations in southern European beech forests, Sci. Total Environ., 775, 145860, https://doi.org/10.1016/j.scitotenv.2021.145860, 2021.

Schaber, J., Badeck, F., Doktor, D., and von Bloh, W.: Combining messy phenological time series, in: Phenological research: methods for environmental and climate change analysis, edited by: Hudson, I. L. and Keatley, M. R., Springer, Dordrecht Heidelberg London New York, 147–158, 2010.

Schwaab, J., Meier, R., Mussetti, G., Seneviratne, S., Bürgi, C., and Davin, E. L.: The role of urban trees in reducing land surface temperatures in European cities, Nat. Commun., 12, 6763, https://doi.org/10.1038/s41467-021-26768-w, 2021.

Singh, R. K., Svystun, T., AlDahmash, B., Jönsson, A. M., and Bhalerao, R. P.: Photoperiod- and temperature-mediated control of phenology in trees – a molecular perspective, New Phytol., 213, 511–524, https://doi.org/10.1111/nph.14346, 2017.

Speich, M. J. R.: Quantifying and modeling water availability in temperate forests: a review of drought and aridity indices, Iforest-Biogeosciences For., 12, 1–16, https://doi.org/10.3832/ifor2934-011, 2019.

Tan, S., Sha, Y., Sun, L., and Li, Z.: Abiotic Stress-Induced Leaf Senescence: Regulatory Mechanisms and Application, Int. J. Mol. Sci., 24, https://doi.org/10.3390/ijms241511996, 2023.

Tang, J. W., Körner, C., Muraoka, H., Piao, S. L., Shen, M. G., Thackeray, S. J., and Yang, X.: Emerging opportunities and challenges in phenology: a review, Ecosphere, 7, 17, https://doi.org/10.1002/ecs2.1436, 2016.

Templ, B., Koch, E., Bolmgren, K., Ungersbock, M., Paul, A., Scheifinger, H., Rutishauser, T., Busto, M., Chmielewski, F. M., Hajkova, L., Hodzic, S., Kaspar, F., Pietragalla, B., Romero-Fresneda, R., Tolvanen, A., Vucetic, V., Zimmermann, K., and Zust, A.: Pan European Phenological database (PEP725): A single point of access for European data, Int J Biometeorol, 62, 1109–1113, https://doi.org/10.1007/s00484-018-1512-8, 2018.

Toomey, M., Friedl, M. A., Frolking, S., Hufkens, K., Klosterman, S., Sonnentag, O., Baldocchi, D. D., Bernacchi, C. J., Biraud, S. C., Bohrer, G., Brzostek, E., Burns, S. P., Coursolle, C., Hollinger, D. Y., Margolis, H. A., McCaughey, H., Monson, R. K., Munger, J. W., Pallardy, S., Phillips, R. P., Torn, M. S., Wharton, S., Zeri, M., and Richardson, A. D.: Greenness indices from digital cameras predict the timing and seasonal dynamics of canopy-scale photosynthesis, Ecol. Appl., 25, 99–115, https://doi.org/10.1890/14-0005.1, 2015.

Van der Meersch, V. and Chuine, I.: Can inverse calibration help improving process-explicit species distribution models?, Ecol. Model., 506, 111132, https://doi.org/10.1016/j.ecolmodel.2025.111132, 2025.

Vicente-Serrano, S. M., Begueria, S., and Lopez-Moreno, J. I.: A Multiscalar Drought Index Sensitive to Global Warming: The Standardized Precipitation Evapotranspiration Index, J. Clim., 23, 1696–1718, https://doi.org/10.1175/2009jcli2909.1, 2010.

Vitasse, Y., Delzon, S., Dufrene, E., Pontailler, J. Y., Louvet, J. M., Kremer, A., and Michalet, R.: Leaf phenology sensitivity to temperature in European trees: Do within-species populations exhibit similar responses?, Agric. For. Meteorol., 149, 735–744, https://doi.org/10.1016/j.agrformet.2008.10.019, 2009.

Vitasse, Y., Hoch, G., Randin, C. F., Lenz, A., Kollas, C., Scheepens, J. F., and Korner, C.: Elevational adaptation and plasticity in seedling phenology of temperate deciduous tree species, Oecologia, 171, 663–678, https://doi.org/10.1007/s00442-012-2580-9, 2013.

Wang, H., Gao, C., and Ge, Q.: Low temperature and short daylength interact to affect the leaf senescence of two temperate tree species, Tree Physiol., 42, 2252–2265, https://doi.org/10.1093/treephys/tpac068, 2022.

Wang, J. and Liu, D.: Larger diurnal temperature range undermined later autumn leaf senescence with warming in Europe, Glob. Ecol. Biogeogr., 32, 734–746, https://doi.org/10.1111/geb.13674, 2023.

Wasserman, L.: All of Statistics. A Concise Course in Statistical Inference, 1st ed., Springer New York, NY, 2004.

Wheeler, K. I. and Dietze, M. C.: A trigger may not be necessary to cause senescence in deciduous broadleaf forests. (Preprint), bioRxiv, 2023.06.07.544057, https://doi.org/10.1101/2023.06.07.544057, 2023.

Wickham, H.: ggplot2: Elegant graphics for data analysis, Springer-Verlag, New York, 2016.

Wickham, H., Hester, J., and Bryan, J.: readr: Read Rectangular Text Data, 2024.

Wood, S. N.: Fast stable restricted maximum likelihood and marginal likelihood estimation of semiparametric generalized linear models, J. R. Stat. Soc. Ser. B Stat. Methodol., 73, 3–36, https://doi.org/10.1111/j.1467-9868.2010.00749.x, 2011.

Wood, S. N.: Generalized additive models: An introduction with R, 2nd edition., Chapman and Hall/CRC, New York, 2017.

Wu, C., Peng, J., Ciais, P., Peñuelas, J., Wang, H., Beguería, S., Andrew Black, T., Jassal, R. S., Zhang, X., Yuan, W., Liang, E., Wang, X., Hua, H., Liu, R., Ju, W., Fu, Y. H., and Ge, Q.: Increased drought effects on the phenology of autumn leaf senescence, Nat. Clim. Change, 12, 943–949, https://doi.org/10.1038/s41558-022-01464-9, 2022.

Xiang, Y., Sun, D. Y., Fan, W., and Gong, X. G.: Generalized Simulated Annealing algorithm and its application to the Thomson model, Phys. Lett. A, 233, 216–220, https://doi.org/10.1016/s0375-9601(97)00474-x, 1997.

Xiang, Y., Gubian, S., Martin, F., Suomela, B., and Hoeng, J.: Generalized Simulated Annealing for Global Optimization: The GenSA Package, R J., 5, 13–28, https://doi.org/10.32614/RJ-2013-002, 2013.

Xiang, Y., Gubian, S., and Martin, F.: Generalized Simulated Annealing, in: Computational Optimization in Engineering - Paradigms and Applications, 25–46, 2017.

Xie, Y., Wang, X. J., and Silander, J. A.: Deciduous forest responses to temperature, precipitation, and drought imply complex climate change impacts, Proc. Natl. Acad. Sci. U. S. A., 112, 13585–13590, https://doi.org/10.1073/pnas.1509991112, 2015.

Xie, Y., Wang, X. J., Wilson, A. M., and Silander, J. A.: Predicting autumn phenology: How deciduous tree species respond to weather stressors, Agric. For. Meteorol., 250, 127–137, https://doi.org/10.1016/j.agrformet.2017.12.259, 2018.

Yates, F.: The analysis of multiple classifications with unequal numbers in the different classes, J. Am. Stat. Assoc., 29, 51–66, https://doi.org/10.2307/2278459, 1934.

Yu, H., Mo, Z., Tan, T., Qiu, L., and Guo, L.: Increased discrepancy between autumn leaf senescence and the end of photosynthesis influenced by climate and spring phenology.

Zani, D., Crowther, T. W., Mo, L., Renner, S. S., and Zohner, C. M.: Increased growing-season productivity drives earlier autumn leaf senescence in temperate trees, Science, 370, 1066–1071, https://doi.org/10.1126/science.abd8911, 2020.

Zargar, A., Sadiq, R., Naser, B., and Khan, F. I.: A review of drought indices, Environ. Rev., 19, 333–349, https://doi.org/10.1139/a11-013, 2011.

Zeileis, A. and Grothendieck, G.: zoo: S3 Infrastructure for Regular and Irregular Time Series, J. Stat. Softw., 14, 1–27, https://doi.org/10.18637/jss.v014.i06, 2005.

Zeng, L., Wardlow, B. D., Xiang, D., Hu, S., and Li, D.: A review of vegetation phenological metrics extraction using time-series, multispectral satellite data, Remote Sens. Environ., 237, 111511, https://doi.org/10.1016/j.rse.2019.111511, 2020.

Zeng, Z. A. and Wolkovich, E. M.: Weak evidence of provenance effects in spring phenology across Europe and North America, New Phytol., 242, 1957–1964, https://doi.org/10.1111/nph.19674, 2024.

Zimmerman, O. R. and Richardson, A. D.: Near-Surface Sensor-Derived Phenology, in: Phenology: An Integrative Environmental Science, edited by: Schwartz, M. D., Springer Nature Switzerland, Cham, 461–478, https://doi.org/10.1007/978-3-031-75027-4_20, 2024.

Zohner, C. M., Mirzagholi, L., Renner, S. S., Mo, L., Rebindaine, D., Bucher, R., Palouš, D., Vitasse, Y., Fu, Y. H., Stocker, B. D., and Crowther, T. W.: Effect of climate warming on the timing of autumn leaf senescence reverses after the summer solstice, Science, 381, eadf5098, https://doi.org/10.1126/science.adf5098, 2023.

670

Supplement to: **Aging _and stress_ explains~~s~~ _the_ earlier ~~start~~onset of leaf senescence in trees ~~during~~in warmer years: translating the latest findings on senescence regulation into the DP3 model (v1.1)**

Michael Meier*[1,2], Christof Bigler[23], Isabelle Chuine[1]

[1] CEFE, Univ Montpellier, CNRS, EPHE, IRD, Montpellier, France

[2] Institute of Earth Surface Dynamics, University of Lausanne, Lausanne, Switzerland

[23] Forest Ecology, Department of Environmental Systems Science, ETH Zurich, Zurich, Switzerland

Correspondence to: Michael Meier, (~~michael.meier@cefe.cnrs.fr~~michael.meier.1@unil.ch)

S1 Data

S1.1 Phenological data

S1.1.1 Coordinate transformation

The coordinates of the Swiss sites (Swiss phenology network, 2025) were transformed from the Swiss LV03 North and East projections (x and y [m]) to WGS84 latitude and longitude (φ and λ [°], respectively; Eqs. S1–S6; Sect. 2 in Geodesy, 2016):

$$x' = (x - 200000\,\text{m})/1000000 \tag{S1}$$

$$y' = (y - 600000\,\text{m})/1000000 \tag{S2}$$

$$\phi' = 2.6779094 + 4.728982\, y' + 0.791484\, y'\, x' + 0.1306\, y'\, x'^2 - 0.0436\, y'^3 \tag{S3}$$

$$\lambda' = 16.9023892 + 3.238272\, x' - 0.270978\, y'^2 - 0.002528\, x'^2 - 0.0447\, y'^2\, x' - 0.0140\, x'^3 \tag{S4}$$

$$\phi = \phi'/0.36 \tag{S5}$$

$$\lambda = \lambda'/0.36 \tag{S6}$$

S1.1.2 Relationship with latitude, longitude, and elevation

We related the average leaf senescence date per site to latitude, longitude, and elevation through linear regression models fitted separately for the average day of year when 50% and 100% of the leaves have turned color or have fallen (average LS50 and average LS100, respectively; Eq. S7; using the function lm in the R package stats; R Core Team, 2025):

$$\mathbf{y} = \mathbf{X}\boldsymbol{\beta} + \boldsymbol{\epsilon} \tag{S7}$$

$\mathbf{y}$ is the n_j-dimensional vector of the response variables average LS_{50} and average LS_{100}, where j refers to either response variable and n_j is the corresponding number of observations. $\mathbf{X}$ is the $n_j \times 4$ matrix with the values of the first column being set to 1 (for the intercept) and the 2nd to 4th columns containing the respective explanatory variables latitude [°], longitude [°], and elevation [m a.s.l.]. $\boldsymbol{\epsilon}$ is the n_j-dimensional vector of normally distributed errors with $N(0, \sigma_j^2)$. Thus, $\boldsymbol{\beta}$ is the 4-dimensional vector of the coefficient estimates for the intercept, latitude, longitude, and elevation.

The linear regression models revealed earlier average leaf senescence dates (i.e., aLS$_{50}$ and aLS$_{100}$) with increasing latitude, increasing longitude, and increasing elevation (Table S1). Inline with recent research, this translates into earlier leaf senescence with cooler and more continental climatic conditions as well as with longer days during summer and faster decrease in day length between summer solstice and winter solstice (e.g., Kloos et al., 2024; Wang et al., 2022; but see Lu and Keenan, 2022).

Table S1. Coefficient estimates of the linear regression models

Response	Explanatory	Estimate	Standard error	t statistic	p-value	Adjusted R^2
average LS$_{50}$ [doy]	Intercept	386.35	21.13	18.2837	0.000000	0.4761
	Latitude [°]	−1.69	0.40	-4.2079	0.000036	
	Longitude [°]	−1.61	0.15	-10.9693	0.000000	
	Elevation [m a.s.l.]	−0.0142	0.0031	-4.5542	0.000008	
average LS$_{100}$ [doy]	Intercept	374.87	36.49	10.2731	0.000000	0.7614
	Latitude [°]	−0.95	0.70	-1.3631	0.175860	
	Longitude [°]	−1.62	0.27	-5.9722	0.000000	
	Elevation [m a.s.l.]	−0.0219	0.0049	-4.4497	0.000022	

Note: The linear regression models were fitted separately to the response variables average LS_{50} and average LS_{100} (i.e., the day of year [doy] when respective 50% and 100% of the leaves have turned color or have fallen). The coefficient estimates of the explanatory variables are given together with the corresponding standard errors, t statistic, and p-values. The adjusted R^2 is given for each model.

S1.2 Driver calculations

S1.2.1 Day length

Day length (L_{doy}) for a given day of year (doy [d]) was calculated from latitude (φ; [°]) according to Eqs. 1, 3, and 4 in Brock (1981; Eqs. S8–S10):

$$L_{doy} = 2 \frac{W_{doy}}{15° \, h^{-1}} \tag{S8}$$

$$W_{doy} = \arccos\left(-\tan\left(\varphi\right) * \tan\left(\gamma_{doy}\right)\right) \tag{S9}$$

$$\gamma_{doy} = 23.45° \sin\left(360° \left(doy - 81\right)/365\right) \tag{S10}$$

With γ_{doy} and W_{doy} being the respective declination [°] and hour-angle [°] at sunrise at doy.

S1.2.2 Photosynthetic activity

Sink limited daily net photosynthetic activity (A_{net} [mol C d^{-1}]; Eq. S11; Collatz et al., 1991) was calculated as the difference between the gross photosynthetic activity (A_{grs} [mol C d^{-1}]) and respiration (R [mol C d^{-1}]; Collatz et al., 1991; Farquhar et al., 1980; Wohlfahrt and Gu, 2015).

$$A_{net} = A_{grs} - R \tag{S11}$$

A_{grs} in turn depended on photon availability (J_E [mol C d^{-1}]), Rubisco activity (J_C [mol C d^{-1}]), and sink capacity (J_S [mol C d^{-1}]; Eq. S12), while R was defined as a fraction of the maximum photosynthetic rate (V_{max} [mol C d^{-1}]; Eq. S13).

$$A_{grs} = \max\left(0, \quad L \times \frac{J_P + J_S - \sqrt{(J_P + J_S)^2 - 4\beta_C J_P J_S}}{2\beta_C}\right) \tag{S12}$$

$$R = b_{C3} V_{max} \tag{S13}$$

J_P is an intermediate variable, combining J_E and J_C (Eq. S14), β_C is a constant shape parameter, and b_{C3} is a constant fraction for C3 plants (Table S1).

$$J_P = \frac{J_C + J_E - \sqrt{(J_C + J_E)^2 - 4\theta_C J_E J_C}}{2\theta_C} \tag{S14}$$

θ_C is a constant shape parameter (Table S1). J_E and J_C are daily fractions of the available photosynthetically active radiation (*APAR* [W m^{-2}]; Eq. S15) and V_{max} (Eq. S16), respectively, while J_S is a constant fraction of V_{max} (Eq. S17).

$$J_E = C_1 \times \frac{APAR}{L} \tag{S15}$$

$$J_C = C_2 \times \frac{V_{max}}{24\,[\text{h}]} \tag{S16}$$

$$J_S = 0.5 \times \frac{V_{max}}{24\,[\text{h}]} \tag{S17}$$

L is the day length [h], and V_{max} depends on *APAR* (Eq. S18), which in turn was calculated as a fraction (*fapar*) of the photosynthetically active radiation (*PAR* [W m^{-2}]; Eq. S19).

$$V_{max} = \frac{1}{b_{C3}} \frac{C_1}{C_2} [(2\theta - 1)s - \sigma(2\theta s - C_2)] APAR \tag{S18}$$

$$APAR = \alpha_a c_q \, fapar \, PAR (3600 \times 24)[s] \tag{S19}$$

θ is a constant shape parameter, while α_a and c_q are a constant ratio and a constant conversion factor for the respective assimilation and conversion of solar radiation (Table S1). While *fapar* depended on the leaf area index (*LAI*; Eq. S20), *PAR* was derived from the surface shortwave down welling radiation (R_s [W m^{-2}]; Eq. S21).

$$fapar = 1 \, e^{-0.5 \, LAI} \tag{S20}$$

$$PAR = 0.5 \, R_s \tag{S21}$$

V_{max} further depends on s and σ (Eqs. S22–S23) as well as on C_1 and C_2 (Eqs. S24–S25).

$$s = b_{C3} \frac{24[h]}{L} \tag{S22}$$

$$\sigma = \sqrt{1 - \frac{C_2 - s}{C_2 - \theta s}} \tag{S23}$$

$$C_1 = \phi_C \alpha_{C3} f(T) \times \frac{p_{i,CO2} - \Gamma_*}{p_{i,CO2} + 2\Gamma^*} \tag{S24}$$

$$C_2 = \frac{(p_{i,CO2} - \Gamma_*)}{p_{i,CO2} + K_C (1 + \frac{p_{a,O2}}{K_O})} \tag{S25}$$

α_{C3} describes the quantum efficiency of C3 plants, and $p_{a,O2}$ is the ambient partial O_2 pressure (Table S1). $p_{i,CO2}$ is the internal partial CO_2 pressure (Eq. S26), Γ_* is the CO_2 condensation point (Eq. S27), K_C and K_O are the kinetic coefficients for CO_2 (Eq. S28) and O_2 (Eq. S29), respectively, and *f(T)* is a function of the mean temperature (Eq. S30).

$$p_{i,CO2} = \lambda_{C3} [CO_2]_A \, 10^{-16} \, p_0 \tag{S26}$$

$$\Gamma_* = \frac{p_{a,O2}}{2 \tau q_{\tau 10}^{(T-25K)/10}} \tag{S27}$$

$$K_C = k_C q_{C10}^{(T-25K)/10} \tag{S28}$$

$$K_O = k_O q_{O10}^{(T-25K)/10} \tag{S29}$$

$$f(x) = \min\left(1, \quad \max\left(0, \quad \frac{1}{1+e^{k_1(k_2-T)}} \times \left(1-0.01\,e^{k_3(T-x_3)}\right)\right)\right) \tag{S30}$$

λ_{C3} is the optimal ratio of internal to ambient CO_2 pressure of C3 plants. τ, k_C, and k_O are the specificity ratio $CO_2{:}O_2$ and the Michaelis constants for CO_2 and O_2, respectively, while $q_{\tau 10}$, q_{C10}, and q_{O10} are the corresponding rates of change due to a 10 K change in mean temperature (T [°C]). k_1, k_2, and k_3 are derived from the cardinal temperatures x_1, x_2, x_3, and x_4 (Eqs. S31–S33, Table S1).

$$k_1 = \frac{2\log(1/0.99-1)}{x_1-x_2} \tag{S31}$$

$$k_2 = (x_1+x_2)/2 \tag{S32}$$

$$k_3 = \log\left(\frac{0.99/0.01}{x_4-x_3}\right) \tag{S33}$$

Table S2. Constants.

Constant	Value	Description	Source
β_C	0.95	Fraction; Co-limitation (shape) parameter for J_P and J_S	Co97, Eq. (A9)
b_{C3}	0.015	Fraction; Leaf respiration per maximum Rubisco capacity for C3 plants	HP96, Table 2
θ_C	0.98	Fraction; Co-limitation (shape) parameter for J_C and J_E	Co97, Eq. (A8)
θ	0.7	Fraction; Alternative co-limitation (shape) parameter for J_C and J_E	Table 2 in HP96
α_a	0.5	Ratio; Assimilated PAR from ecosystem to leaf level	Table 4 in Si00
c_q	4.6×10^{-6}	[E J^{-1}], [mol J^{-1}]; Conversion factor for solar radiation at 550 nm	
α_{C3}	0.08	Intrinsic quantum efficiency of CO_2 uptake in C3 plants	Ha96; Si00
p_0	1.013×10^5	[Pa]; Standard pressure	-
$P_{a,O2}$	$0.209 \times p_0$	[Pa]; Ambient O_2 pressure	Table A1 in Co97; Table 2 in HP96
λ_{C3}	0.8	Fraction	Ge04
τ	2600	Ratio; $CO_2{:}O_2$ specificity ratio	Table A1 in Ca91
k_O	3×10^4	[Pa]; Michaelis constant for O_2	Table A1 in Co97; Table 2 in HP96
k_C	30	[Pa]; Michaelis constant for CO_2	
$q_{\tau 10}$	0.57	Fraction; Temperature-sensitivity of τ regarding a change of 10 K	Table A1 in Ca91
q_{O10}	1.2	Fraction; Temperature-sensitivity of k_O regarding a change of 10 K	Table A1 in Co97; Table 2 in HP96
q_{C10}	1.2	Fraction; Temperature-sensitivity of k_C regarding a change of 10 K	
x_1	1	[°C]; Cardinal temperatures	Eqs. S10–S15 in Za20
x_2	18		
x_3	25		
x_4	45		

Note: These constants were taken from the following sources: Co91: (Collatz et al., 1991); Ge04: (Gerten et al., 2004); Ha96: (Haxeltine et al., 1996); HP96: (Haxeltine and Prentice, 1996); Si00: (Sitch et al., 2000); Za20: (Zani et al., 2020).

S1.2.3 Keetch and Byram drought index

The Keetch and Byram drought index for day i (Q_i; Eq. S34) was calculated from daily precipitation (P_i) and daily maximum temperature (Tx_i; Keetch and Byram, 1968), which were converted from millimeters [mm] to inches [in] and from degree Celsius [°C] to degree Fahrenheit [°F], respectively (P'_i and Tx'_i; Eqs. S35–S36; Foster et al., 1981, Table 2; Shaw, 1931; Woods, 1931):

$$Q_i = \min\left(800, \quad \max\left(0, \quad Q_{Base,i} + \Delta Q_i\right)\right) \tag{S34}$$

$$P'_i = \frac{P_i}{25.4\left[\text{mm in}^{-1}\right]} \tag{S35}$$

$$Tx'_i = 9/5\left[\text{°F °C}^{-1}\right] \times Tx_i + 32\left[\text{°F}\right] \tag{S36}$$

The base index ($Q_{base,i}$) was derived from Q of the previous day (i.e., Q_{i-1}) and the net precipitation of the given day ($P_{net,i}$ [in]; Eq. S37), while the daily drought factor (ΔQ_i) was calculated from the base index ($Q_{base,i}$), Tx'_i, and mean annual rainfall (R_i, [in]; Eqs. S38–S39):

$$Q_{Base,i} = \max\left(0, \quad Q_{i-1} - 100\, P_{net,i}\right) \tag{S37}$$

$$\Delta Q_i = \left(800 - Q_{Base,i}\right) \times \frac{0.968\, e^{0.0486\, Tx'_i} - 0.83}{1 + 10.88\, e^{-0.0441\, R_i}} \times 0.001 \tag{S38}$$

$$R_i = \frac{1}{366} \sum_{j=i-355}^{i} P'_j \tag{S39}$$

Here, $Q_{Base,1}$ (i.e., of January 1st, 1950) was set to the average Q_{Base} during the Decembers and Januaries of 1955–1959, $R_1, R_2, ..., R_{355} = R_{366}$, and $P'_i = 0$ if the precipitation fell as snow (i.e., if the mean temperature $T_i \leq 0$ °C). P_{net} depends on P' of the given and two previous days in comparison to a threshold precipitation of 0.2 in (Y_P; Eq. S40).

$$P_{net,i} = \begin{cases} \max\left(0, \quad P'_i - Y_P\right) & , \quad if \quad P'_{i-1} = 0 \\ P'_i & , \quad if \quad P'_{i-1} \geq Y_P \\ \max\left(0, \quad \sum_{k=0}^{1} P'_{i-k} - Y_P\right) & , \quad if \quad P'_{i-1} < Y_P \quad \wedge \quad \sum_{k=1}^{2} P'_{i-k} \geq Y_P \\ \max\left(0, \quad \sum_{k=0}^{2} P'_{i-k} - Y_P\right) & , \quad if \quad P'_{i-1} < Y_P \quad \wedge \quad \sum_{k=1}^{2} P'_{i-k} < Y_P \end{cases} \tag{S40}$$

The KBDI was initiated per site, i.e., setting Q_i to zero after the first period of either abundant precipitation or snow melt during 1950–1954 (Keetch and Byram, 1968). A period of abundant precipitation was defined as seven consecutive days during which the precipitation sum was six inches (i.e., 152.4 mm; see Eq. S34) or more. A period of snow melt was defined as four consecutive days during which the snow melt followed on at least seven days with snow

fall. For this, we defined day i as a day with snow melt when $T_i > 0$ °C and as a day with snow fall when $P_i > 0$ mm and $T_i \leq 0$ °C.

S2 Methods

S2.1 Initial ranges for parameters

Table S3. Ranges for parameter calibration

Symbol	Meaning	Boundaries
$-a_C$	Boundary below which cold stress is 1 versus 0	0–30 °C
$b_{0,C}$	Boundary above which cold stress gradually increases from 0 to 1	0–30 °C
$b_{1,C}$	Boundary below which cold stress gradually decreases from 1 to 1	$(b_{0,C}+0$ °C$)$–$(b_{0,C}+20$ °C$)$
$-a_P$	Boundary below which photoperiod stress is 1 versus 0	–0.25–+0.25 h
$b_{0,P}$	Boundary above which photoperiod stress gradually increases from 0 to 1	–0.25–+0.25 h
$b_{1,P}$	Boundary below which photoperiod stress gradually decreases from 1 to 0	$(b_{0,P}+0$ h$)$–$(b_{0,P}+0.3$ h$)$
a_D	Boundary above which dry stress is 1 versus 0	0–800
$-b_{0,D}$	Boundary above which dry stress gradually increases from 0 to 1	0–800
$-b_{1,D}$	Boundary below which dry stress gradually decreases from 1 to 0	$(b_{0,D}+0)$–$(b_{0,D}+400)$
a_R	Boundary above which rain stress is 1 versus 0	0–500 mm
$-b_{0,R}$	Boundary above which rain stress gradually increases from 0 to 1	0–500 mm
$-b_{1,R}$	Boundary below which rain stress gradually decreases from 1 to 0	$(b_{0,R}+0$ mm$)$–$(b_{0,R}+300$ mm$)$
a_H	Boundary above which heat stress is 1 versus 0	25–50 °C
a_N	Boundary above which nutrient stress is 1 versus 0	20–250 mol C d^{-1}
$-a_F$	Boundary below which frost stress is 1 versus 0	–5–+10 °C
w_C	Weight of cold stress	0–1
w_P	Weight of photoperiod stress	0–1
w_D	Weight of dry stress	0–1
w_R	Weight of rain stress	0–1
w_H	Weight of heat stress	0–1
w_N	Weight of nutrient stress	0–1
w_F	Weight of frost stress	0–1
w_A	Weight of aging rate	0–1
w_S	Weight of stress rate	0–1
s_X	Scaling factor of the senescence rate	0–1
x_S	Shape parameter of the stress rate	0–10
c	First parameter of exponential function	0.005–0.5
d	Second parameter of exponential function	0–15
$Y_{Aging,1}$	Threshold for the aging state, marking the transition from young to mature leaf	0–50 d
$Y_{Aging,2}$	Threshold for the aging state, marking the transition from mature to old leaf	$(Y_{Aging,1}$~~+0 d~~$)$–$(Y_{Aging,1}+250$ d$)$
Y_{LS100}	Threshold for the senescence state, indicating the day of LS$_{100}$	0–10

Note: The symbols of the parameters for the boundaries below or above which stress occurs [a; see response function $g(x)$; Eq. 7], for the boundaries between which stress occurs [b_0 and b_1; see response function $h(x)$; Eq. 8], and for the weights (w) that define the stress rate as well as for the different formulations of the senescence rate (w_A, w_S, s_X, x_S, c, and d; Eq. 9) and the thresholds (Y) that mark the transitions from young to mature leaf, the transition from mature to old leaf and the time when 100% of the leaves have changed color or have fallen (LS_{100}).

S2.2 Controls of the simulated annealing algorithm

The choice of the controls for the optimization algorithm influences the accuracy of the calibrated model (Meier and Bigler, 2023) through the exploration–exploitation trade-off (Candelieri, 2021; Maes et al., 2013). Thus, we set the controls 'maximum iterations', 'maximum calls', and 'temperature' of the generalized simulated annealing algorithm (Xiang et al., 1997, 2017) in such a way that the calibrated model resulted in most accurate ~~simulations~~predictions for the

validation sample. To identify these optimal controls for each model and calibration sample, we calibrated each model four times (i.e., twice with each sample draw) with all 27 combinations of 4000, 5000, and 6000 maximum iterations, 10^6, 10^7, and 10^8 maximum calls, as well as temperatures of 5200, 5230, and 5300. Thus, we used the combination of controls that resulted in the lowest average Akaike information criterion for small samples (i.e., $n < 40k$; AICc; Eq. S41; based on the validation sample; Akaike, 1974; Burnham and Anderson, 2004) to compute the additional six calibration runs (i.e., three per calibration sample; Table S4).

$$AICc = AIC + \frac{2k(k+1)}{n-k-1} \tag{S41}$$

$$AIC = -2 \times \log(L) + 2k \tag{S42}$$

$$\sigma_e = \sqrt{\frac{1}{n} \sum_{i=1}^{n} (x_{p,i} - x_{o,i})^2} \tag{S43}$$

n is the number of <u>predicted and </u>observed ~~and simulated~~ doy pairs (x_{p} and x_{o}, respectively) and k is the number of free model parameters. L is the likelihood for the normally distributed model errors (i.e., $x_p - x_o$; Fisher and Russell, 1997) with $N(0, \sigma_e)$. In case $S_{Senescence}$ did not reach the thresholds $Y_{LS_{50}}$ and $Y_{LS_{100}}$ until December 31st, corresponding x_{p} were considered missing and thus set to doy 367 before their accuracy was evaluated.

Table S4. Optimal controls of the generalized simulated annealing algorithm.

Model	Sample	Maximum iterations	Maximum calls	Temperature
CDD	LS$_{50}$	4000	10^8	5300
DM2	LS$_{50}$	6000	10^6	5300
PIA	LS$_{50}$	5000	10^7	5200
DP3	LS$_{50}$	4000	10^8	5300
	LS$_{50}$-LS$_{100}$	5000	10^7	5200

Note: Only the control settings for the evaluated models (LS$_{50}$ sample) and for the model that was selected through the iterations of model development (LS$_{50}$-LS$_{100}$ sample) are shown. Those for the models that were rejected during model development are omitted.

S2.3   Model calibration, selection, and evaluation

All models were calibrated by minimizing the root mean squared error (RMSE; Eq. S44).

$$RMSE = \sqrt{\frac{1}{n} \sum_{i=1}^{n} (x_{p,i} - x_{o,i})^2} \tag{S44}$$

Thus, for each model, we selected and further evaluated the calibration run that resulted in highest modified Kling-Gupta efficiency (KGE'; Eq. S45; Gupta et al., 2009; Kling et al., 2012) for the validation sample.

$$KGE' = 1 - \sqrt{(\rho - 1)^2 + (\beta - 1)^2 - (\gamma - 1)^2} \tag{S45}$$

$$\beta = \mu_p \Big/ \mu_o \tag{S46}$$

$$\gamma = \frac{\sigma_p / \mu_p}{\sigma_o / \mu_o} \tag{S47}$$

β is the bias ratio, γ is the variability ratio, and ρ is the Pearson correlation between x_{ip} and x_{io}. μ_{ip} and μ_{io}, are the respective predicted and observed ~~and simulated~~ mean doy, and σ_{ip} and σ_{io} are the corresponding standard deviations. For the perfect model (i.e., $x_{ip} = x_{io}$ for all i), $\rho = 1$, $\beta = 1$, and $\gamma = 1$, and thus $KGE' = 1$, whereas $1 > KGE' > -\infty$ for imperfect models.

S2.4 Linear mixed-effects model and analysis of variance

We fitted a linear mixed-effects model (LMM; Eq. S48; Pinheiro and Bates, 2000; Wood, 2011, 2017) to analyze the effects on the model error:

$$\mathbf{y} = \mathbf{X}\boldsymbol{\beta} + \mathbf{Z}\mathbf{b} + \boldsymbol{\epsilon} \tag{S48}$$

$\mathbf{y}$ is the n-dimensional vector of the response variable 'model error' (ME) and n is the corresponding number of ME. $\mathbf{X}$ is the $n \times p$ matrix of the intercept (i.e., 1) and the $p - 1$ explanatory variables. $\boldsymbol{\beta}$ is the corresponding p-dimensional vector of the fixed effects 'country' and 'model' as well as the annual and site-specific deviations in mean annual temperature, mean annual KBDI, accumulated A_{net} between LU and summer solstice, latitude, and elevation (CTR, MOD, δMAT, δMAQ, δA_{net}, δLAT and δELV, respectively) from the overall calibration sample means per variable. $\mathbf{Z}$ is the $n \times q$ matrix of the random effects, assigning the n observations to the q groups of the grouping variable 'site' (STE). $\mathbf{b}$ is the corresponding q-dimensional vector of the random intercepts with $\mathbf{b} \sim N(0, \sigma_{\mathbf{b}}^2 \mathbf{I}_q)$, and $\boldsymbol{\epsilon}$ is the n-dimensional vector of the errors with $\boldsymbol{\epsilon} \sim N(0, \sigma^2 \mathbf{I}_n)$ (Baayen et al., 2008; Chpt. 2.1 in Pinheiro and Bates, 2000; Chpt. 6.2 in Wood, 2017).

We fitted this LMM with the function bam in the R package mgcv (Wood, 2017), using the following formula (Eq. S49):

```
ME ~ MOD * (δMAT + δMAQ + δAnet + δLAT + δELV) + CTR + s(STE, bs = 're')    (S49)
```

This LMM combined model effects interacting with effects due to climatic deviations from the calibration sample (red), spatial deviations from the calibration sample (green), and data structure (blue). The LMM was the basis for the type-III ANOVA (Yates, 1934), which we derived with the functions aov and drop1 in the R package stats (Eq. S50; R Core Team, 2025):

```
drop1(aov(LMM), scope = ~., test = "F")    (S50)
```

Thus, we calculated the amount of variation attributed to differences among each explanatory variable, i.e., the relative impact of given variable on the variance in the model error explained by the LMM, by dividing the variable-specific sum of squares by the total sum of squares over all variables.

S3   Results

S3.1   Formulation of the leaf development process

Figure S1. Tested models. The tested models were labeled according to their formulation, namely as $x_P\_x_A\_x_S\_x_X$, with x_P being the number of leaf development phases (i.e., 2 or 3), x_A being the driver of the aging rate (i.e., A or D for photosynthesis or days, respectively), x_S being the stress rate in response [i.e., g or h for $g(x)$ or $h(x)$] to the stressors cold (C), shortening (P), dry (D), heat (H), and frost (F) days, heavy rain periods (R), and nutrient depletion (N), and x_X indicating the formulation of the senescence rate (i.e., S, P, or X when formulated as a sum, product, or exponential function of aging and stress, respectively). After each iteration, we identified the two most accurate models across the given and all previous iterations (Fig, 5, Sect. 2.5). These models were further developed through the next iteration. As soon as such a subsequent iteration did not produce any new model, we selected the most accurately formulated model among all iterations (bold; i.e., the 'DP3' model). All models were tested for beech based on the LS_{50}-LS_{100} sample (Sect. 2.4).
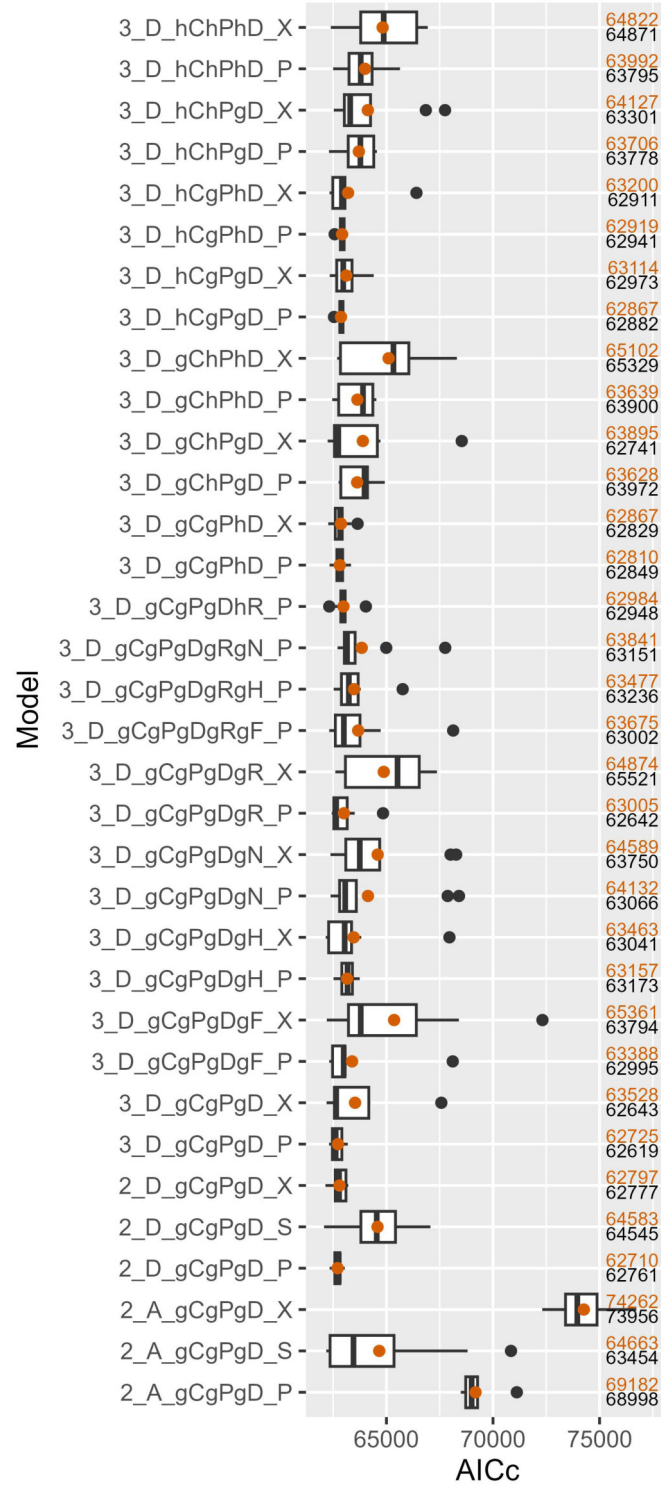
Figure S2. Accuracy of the tested model formulations. The accuracy was assessed with the Akaike information criterion for small samples (AICc; Eq. S40). The boxes indicate the inner quartile range and the median (middle line). The most extreme values are indicated with dots if outside ±1.5 times the inner quartile range from the 1st and 3rd quartile, and with whiskers otherwise. Orange dots show the mean, which is further indicated in orange to the right of each box, together with the median indicated in black. The models were labeled as $x_P\_x_A\_x_S\_x_X$, with x_P being the number of leaf development phases (i.e., 2 or 3), x_A being the driver of the aging rate (i.e., A or D for photosynthesis or days, respectively), x_S being the stress rate that is the summed response [i.e., g or h for *g(x)* or *h(x)*] to the stressors cold (C), shortening (P), dry (D), heat (H), and frost days (F), heavy rain periods (R), and nutrient depletion (N), and x_X indicating the formulation of the senescence rate (i.e., S, P, or X when formulated as a sum, product, or exponential function of aging and stress, respectively). All models were calibrated with the LS$_{50}$-LS$_{100}$ sample (Sect. 2.4).

Table S5. Senescence summarized across mean annual temperature

Calibration	Subject	Variable	3.8–6.1 °C	6.1–8.4 °C	8.4–10.7 °C	10.7–13.0 °C	13.0–15.4 °C
LS_{50}-LS_{100}	Size	Site-years	329	2325	3652	570	48
	Timing	SI [doy]	172.90	164.42	156.36	151.31	149.42
		LS_{50} [doy]	291.86	291.20	288.15	282.21	270.65
		LS_{100} [doy]	290.30	290.05	291.77	296.65	-
	Duration	LS_{50}–SI [d]	118.96	126.80	131.79	130.92	121.23
		LS_{100}–SI [d]	123.90	123.94	134.81	144.23	-
	Cause	Stress	0.77	0.66	0.61	0.66	0.94
		Aging	0.21	0.33	0.38	0.33	0.04
		Both	0.02	0.01	0.01	0.01	0.02
	Stressors SI	Cold	0.46	0.52	0.41	0.28	0.15
		Photoperiod	0.54	0.48	0.58	0.71	0.85
		Dry	0.00	0.00	0.01	0.01	0.00
	Stressors LS_{50}	Cold	0.56	0.64	0.57	0.41	0.12
		Photoperiod	0.44	0.36	0.42	0.59	0.88
		Dry	0.00	0.00	0.00	0.01	0.00
	Stressors LS_{100}	Cold	0.06	0.11	0.15	0.20	-
		Photoperiod	0.94	0.89	0.85	0.80	-
		Dry	0.00	0.00	0.00	0.00	-
LS_{50}	Size	Site-years	334	2346	3620	542	45
	Timing	SI [doy]	132.15	124.48	116.44	111.36	109.51
		LS_{50} [doy]	282.96	283.43	283.36	282.98	282.84
	Duration	LS_{50}–SI [d]	150.81	158.95	166.92	171.62	173.33
	Cause	Stress	0.99	1.00	0.96	0.91	0.93
		Aging	0.01	0.00	0.03	0.07	0.07
		Both	0.01	0.00	0.01	0.02	0.00
	Stressors SI	Cold	0.09	0.15	0.26	0.40	0.38
		Photoperiod	0.91	0.85	0.74	0.60	0.62
		Dry	0.00	0.00	0.00	0.00	0.00
	Stressors LS_{50}	Cold	0.00	0.00	0.00	0.01	0.01
		Photoperiod	1.00	1.00	1.00	0.99	0.99
		Dry	0.00	0.00	0.00	0.00	0.00

Note: The summary is structured in the subjects bin size ('size'), timing, duration, cause, and stressors. Size is given by the count of the evaluated variable site-years. Timing is indicated by the mean day of year [doy] of senescence induction (SI) and of the stages when 50% and 100% of the leaves have turned color or have fallen (LS_{50} and LS_{100}, respectively). Duration refers to the periods from SI to LS_{50} and to LS_{100} (LS_{50}–SI and LS_{100}–SI, respectively) and is given in days [d]. Cause is assessed by the relative number of site-years during which aging versus stress induced senescence (i.e., reached their thresholds first), while the variable both refers to aging and stress reaching their thresholds on the same day. Stressors (i.e., cold stress, photoperiod stress, and dry stress) are compared by their relative contribution to the stress rate that has accumulated by SI, LS_{50}, and LS_{100}. The underlying model was calibrated with the LS_{50}-LS_{100} and LS_{50} samples (Sect. 2.4).

Table S6. Senescence summarized across mean annual Keetch and Byram drought index

Calibration	Subject	Variable	2.7–23.5	23.5–44.2	44.2–65.0	65.0–85.7	85.7–107.0
LS_{50}-LS_{100}	Size	Site-years	6603	270	45	4	2
	Timing	SI [doy]	159.65	154.16	153.60	156.50	150.00
		LS_{50} [doy]	288.63	290.92	291.98	297.00	291.50
		LS_{100} [doy]	291.15	292.92	303.33	-	-
	Duration	LS_{50}–SI [d]	128.98	136.73	138.34	140.50	141.50
		LS_{100}–SI [d]	129.21	139.84	148.67	-	-
	Cause	Stress	0.65	0.50	0.36	0.50	0.50
		Aging	0.34	0.49	0.64	0.50	0.50
		Both	0.01	0.00	0.00	0.00	0.00
	Stressors SI	Cold	0.43	0.56	0.74	0.79	0.50
		Photoperiod	0.56	0.43	0.26	0.21	0.50
		Dry	0.01	0.00	0.00	0.00	0.00
	Stressors LS_{50}	Cold	0.57	0.71	0.77	0.92	1.00
		Photoperiod	0.43	0.29	0.23	0.08	0.00
		Dry	0.00	0.00	0.00	0.00	0.00
	Stressors LS_{100}	Cold	0.13	0.14	0.35	-	-
		Photoperiod	0.87	0.86	0.65	-	-
		Dry	0.00	0.00	0.00	-	-
LS_{50}	Size	Site-years	6578	263	39	5	2
	Timing	SI [doy]	119.76	113.81	113.77	116.00	110.00
		LS_{50} [doy]	283.32	283.64	283.08	285.00	284.50
	Duration	LS_{50}–SI [d]	163.56	169.83	169.31	169.00	174.50
	Cause	Stress	0.97	0.94	0.85	1.00	1.00
		Aging	0.02	0.04	0.13	0.00	0.00
		Both	0.01	0.02	0.03	0.00	0.00
	Stressors SI	Cold	0.22	0.32	0.22	0.04	0.61
		Photoperiod	0.78	0.68	0.78	0.96	0.39
		Dry	0.00	0.00	0.00	0.00	0.00
	Stressors LS_{50}	Cold	0.00	0.00	0.00	0.00	0.00
		Photoperiod	1.00	1.00	1.00	1.00	1.00
		Dry	0.00	0.00	0.00	0.00	0.00

Note: See Table S5.

Table S7. Senescence summarized across latitude

Calibration	Subject	Variable	45.8–48.3 °N	48.3–50.7 °N	50.7–53.1 °N	53.1–55.6 °N	55.6–58 °N
LS_{50}-LS_{100}	Size	Site-years	3709	1792	884	512	27
	Timing	SI [doy]	160.66	157.82	157.32	159.14	160.96
		LS_{50} [doy]	283.32	294.36	294.96	298.69	275.42
		LS_{100} [doy]	289.14	295.61	296.53	293.06	290.43
	Duration	LS_{50}–SI [d]	122.66	136.52	137.58	139.65	114.54
		LS_{100}–SI [d]	124.34	141.34	141.64	135.67	130.33
	Cause	Stress	0.79	0.48	0.48	0.42	0.96
		Aging	0.21	0.51	0.51	0.57	0.04
		Both	0.01	0.01	0.01	0.01	0.00
	Stressors SI	Cold	0.30	0.64	0.58	0.64	0.13
		Photoperiod	0.70	0.36	0.41	0.35	0.87
		Dry	0.01	0.00	0.01	0.00	0.00
	Stressors LS_{50}	Cold	0.41	0.78	0.72	0.89	0.19
		Photoperiod	0.59	0.21	0.28	0.11	0.81
		Dry	0.00	0.00	0.00	0.00	0.00
	Stressors LS_{100}	Cold	0.10	0.14	0.20	0.17	0.10
		Photoperiod	0.90	0.86	0.80	0.83	0.90
		Dry	0.00	0.00	0.00	0.00	0.00
LS_{50}	Size	Site-years	3722	1739	887	511	28
	Timing	SI [doy]	120.85	117.89	117.16	119.05	120.68
		LS_{50} [doy]	283.29	283.37	283.43	283.34	283.71
	Duration	LS_{50}–SI [d]	162.44	165.47	166.27	164.29	163.04
	Cause	Stress	0.98	0.96	0.96	0.97	1.00
		Aging	0.02	0.03	0.03	0.03	0.00
		Both	0.01	0.01	0.01	0.01	0.00
	Stressors SI	Cold	0.21	0.26	0.25	0.22	0.12
		Photoperiod	0.79	0.74	0.75	0.78	0.88
		Dry	0.00	0.00	0.00	0.00	0.00
	Stressors LS_{50}	Cold	0.00	0.00	0.00	0.00	0.00
		Photoperiod	1.00	1.00	1.00	1.00	1.00
		Dry	0.00	0.00	0.00	0.00	0.00

Note: See Table S5.

Table S8. Senescence summarized across elevation

Calibration	Subject	Variable	−1–288 m	288–576 m	576–864 m	864–1150 m	1150–1440 m
LS_{50}-LS_{100}	Size	Site-years	2023	2767	1329	666	139
	Timing	SI [doy]	156.43	157.27	162.20	168.12	176.01
		LS_{50} [doy]	293.58	287.55	282.78	287.59	305.68
		LS_{100} [doy]	293.29	289.58	290.45	289.03	-
	Duration	LS_{50}–SI [d]	137.14	130.28	120.62	119.47	129.67
		LS_{100}–SI [d]	137.61	131.46	123.19	123.08	-
	Cause	Stress	0.48	0.64	0.81	0.76	0.65
		Aging	0.50	0.35	0.19	0.23	0.33
		Both	0.01	0.01	0.01	0.01	0.01
	Stressors SI	Cold	0.55	0.41	0.32	0.41	0.77
		Photoperiod	0.44	0.59	0.67	0.58	0.23
		Dry	0.00	0.01	0.00	0.00	0.00
	Stressors LS_{50}	Cold	0.74	0.54	0.43	0.50	0.87
		Photoperiod	0.26	0.46	0.56	0.49	0.13
		Dry	0.00	0.00	0.00	0.00	0.00
	Stressors LS_{100}	Cold	0.16	0.13	0.12	0.06	-
		Photoperiod	0.84	0.87	0.88	0.94	-
		Dry	0.00	0.00	0.00	0.00	-
LS_{50}	Size	Site-years	2018	2687	1368	681	133
	Timing	SI [doy]	116.42	117.43	122.23	128.10	135.60
		LS_{50} [doy]	283.32	283.33	283.40	283.25	283.29
	Duration	LS_{50}–SI [d]	166.90	165.90	161.17	155.15	147.68
	Cause	Stress	0.95	0.97	0.98	1.00	1.00
		Aging	0.04	0.02	0.01	0.00	0.00
		Both	0.01	0.01	0.01	0.00	0.00
	Stressors SI	Cold	0.28	0.25	0.17	0.12	0.05
		Photoperiod	0.72	0.75	0.83	0.88	0.95
		Dry	0.00	0.00	0.00	0.00	0.00
	Stressors LS_{50}	Cold	0.00	0.00	0.00	0.00	0.00
		Photoperiod	1.00	1.00	1.00	1.00	1.00
		Dry	0.00	0.00	0.00	0.00	0.00

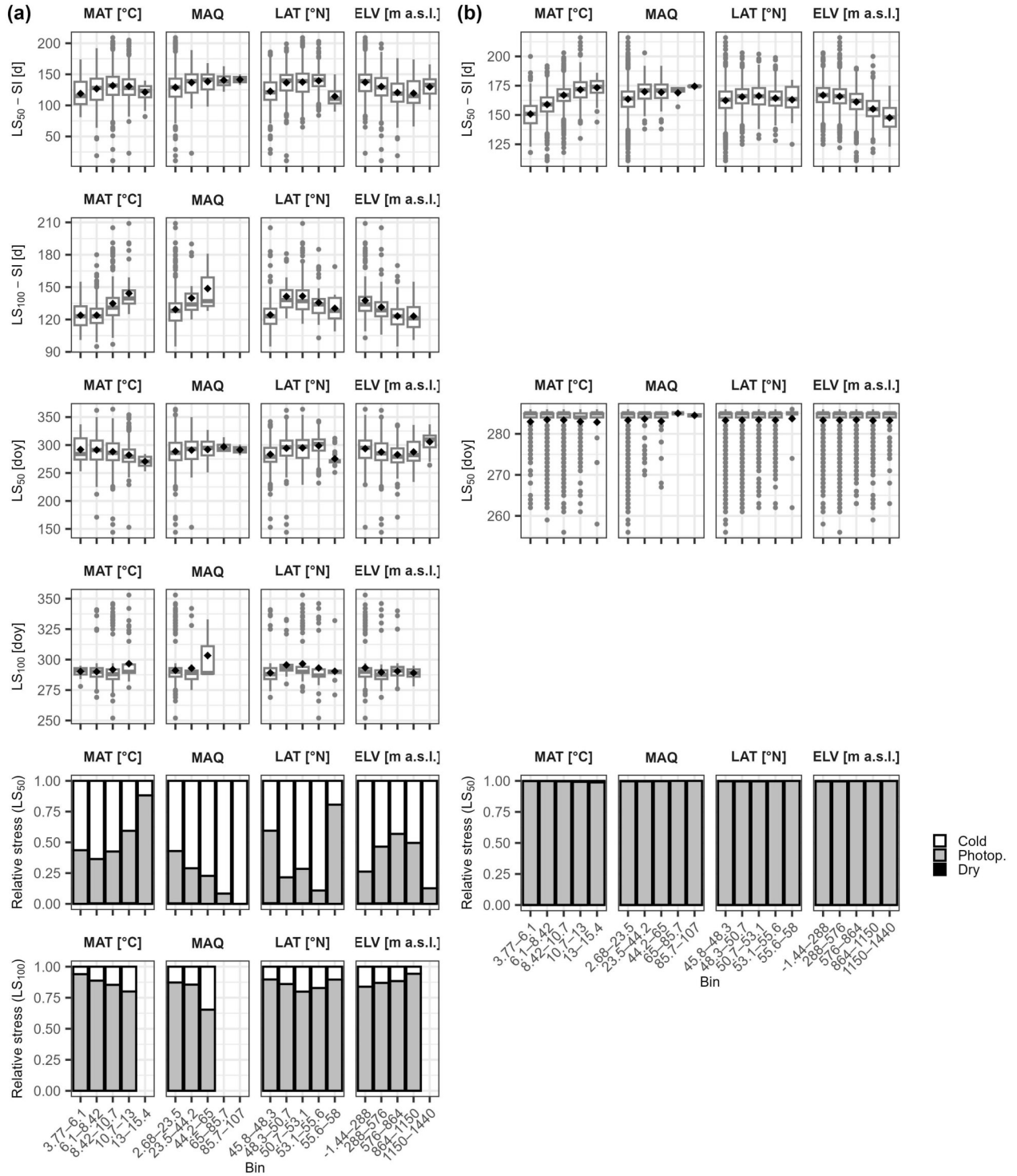*Note*: The bins of elevation are given in m a.s.l.. For further notes see Table S5.

Figure S3. Date and duration of senescence. Panel (a) and (b) are based on ~~simulations~~predictions by the DP3 model calibrated with the LS$_{50}$-LS$_{100}$ versus LS$_{50}$ ~~versus LS$_{50}$ LS$_{100}$~~samples, respectively (Sect. 2.4). The top row of each panel illustrates the duration of senescence according to LS$_{50}$ (i.e., the difference in days [d] of the day when 50% of the leaves have turned color or have fallen, LS$_{50}$, minus the day of senescence induction, SI). The second row of panel (a) shows the duration of senescence according to LS$_{100}$ (i.e., the difference in days [d] of the day when 100% of the leaves have turned color or have fallen, LS$_{100}$, minus SI). The third row of panel (a) and the middle row of panel (b) visualize the day of year [doy] of LS$_{50}$, while the fourth row of panel (a) do so for LS$_{100}$. The fifth row of panel (a) and the bottom row of panel (b) illustrate the relative amount of cold stress, photoperiod stress, and dry stress that accumulated between SI and LS$_{50}$. Accordingly, the bottom row of panel (a) shows these relative amounts for the period from SI to LS$_{100}$. In every row, the x-axis is divided in equally distributed bins among mean annual temperature (MAT, °C), mean annual Keetch and Byram drought index (MAQ), latitude (LAT, °N), and elevation (ELV; m a.s.l.). While the mean and median dates are marked with black dots and grey lines, respectively, the most extreme values are indicated with dots if outside ±1.5 times the inner quartile range from the 1st and 3rd quartile, and with whiskers otherwise.

S3.2 Model error

Table S9. Linear mixed-effects model (LMM) explaining the model error

Coefficient	Value	SE	*t* statistic	*p*-value	$\underline{BF}_{01}$	Lower 0.5%	Upper 99.5%
Intercept	8.1104	1.5297	5.3021	**0.0000**	**0.0000**	4.1700	12.0507
CDD [d]	−1.8144	0.2367	−7.6656	**0.0000**	**0.0000**	−2.4241	−1.2047
DM2 [d]	−0.7348	0.2367	−3.1043	**0.0019**	0.0414	−1.3445	−0.1251
PIA [d]	−0.6290	0.2509	−2.5069	0.0122	0.1785	−1.2754	0.0173
DP3$_{LS_{50}}$ [d]	0.1038	0.2367	0.4385	0.6610	1.0000	−0.5059	0.7135
δMAT [d °C^{-1}]	−2.0028	0.1306	−15.3347	**0.0000**	**0.0000**	−2.3393	−1.6664
δMAQ [d]	0.0901	0.0179	5.0172	**0.0000**	**0.0000**	0.0438	0.1363
δA_{net} [d mol C^{-1} m^{-2}]	0.4148	0.0160	25.9480	**0.0000**	**0.0000**	0.3736	0.4560
δLAT [d °$^{-1}$]	2.1126	0.4724	4.4725	**0.0000**	**0.0003**	0.8959	3.3294
δELV [d m^{-1}]	0.0113	0.0031	3.6690	**0.0002**	*0.0072*	0.0034	0.0193
SUI [d]	−6.1036	1.8142	−3.3643	**0.0008**	0.0193	−10.7770	−1.4302
GER [d]	−7.8265	2.2319	−3.5067	**0.0005**	0.0124	−13.5758	−2.0772
GBR [d]	−24.6277	2.9215	−8.4297	**0.0000**	**0.0000**	−32.1534	−17.1020
CDD × δMAT [d °C^{-1}]	−0.1457	0.1887	−0.7720	0.4401	1.0000	−0.6318	0.3404
DM2 × δMAT [d °C^{-1}]	−0.1771	0.1887	−0.9386	0.3480	1.0000	−0.6632	0.3090
PIA × δMAT [d °C^{-1}]	0.0961	0.1888	0.5092	0.6106	1.0000	−0.3901	0.5824
DP3$_{LS_{50}}$ × δMAT [d °C^{-1}]	−0.0431	0.1887	−0.2283	0.8194	1.0000	−0.5292	0.4430
CDD × δMAQ [d]	−0.0537	0.0276	−1.9495	0.0512	0.4806	−0.1247	0.0173
DM2 × δMAQ [d]	−0.0502	0.0276	−1.8225	0.0684	0.5709	−0.1212	0.0208
PIA × δMAQ [d]	−0.0474	0.0281	−1.6869	0.0916	0.6704	−0.1197	0.0250
DP3$_{LS_{50}}$ × δMAQ [d]	−0.0147	0.0276	−0.5332	0.5939	1.0000	−0.0857	0.0563
CDD × δA_{net} [d mol C^{-1} m^{-2}]	0.0173	0.0236	0.7323	0.4640	1.0000	−0.0435	0.0781
DM2 × δA_{net} [d mol C^{-1} m^{-2}]	0.0093	0.0236	0.3958	0.6922	1.0000	−0.0515	0.0702
PIA × δA_{net} [d mol C^{-1} m^{-2}]	0.0466	0.0236	1.9739	0.0484	0.4639	−0.0142	0.1074
DP3$_{LS_{50}}$ × δA_{net} [d mol C^{-1} m^{-2}]	−0.0031	0.0236	−0.1327	0.8945	1.0000	−0.0639	0.0577
CDD × δLAT [d °$^{-1}$]	−0.0573	0.1376	−0.4162	0.6773	1.0000	−0.4117	0.2972
DM2 × δLAT [d °$^{-1}$]	−0.0665	0.1376	−0.4830	0.6291	1.0000	−0.4209	0.2880
PIA × δLAT [d °$^{-1}$]	−0.0344	0.1378	−0.2495	0.8030	1.0000	−0.3892	0.3205
DP3$_{LS_{50}}$ × δLAT [d °$^{-1}$]	0.0172	0.1376	0.1252	0.9004	1.0000	−0.3372	0.3716
CDD × δELV [d m^{-1}]	−0.0012	0.0013	−0.9438	0.3453	1.0000	−0.0045	0.0021
DM2 × δELV [d m^{-1}]	−0.0011	0.0013	−0.8856	0.3759	1.0000	−0.0044	0.0021
PIA × δELV [d m^{-1}]	−0.0014	0.0013	−1.0789	0.2806	0.9940	−0.0046	0.0019
DP3$_{LS_{50}}$ × δELV [d m^{-1}]	0.0000	0.0013	0.0139	0.9889	1.0000	−0.0032	0.0033

Note: The LMM was fitted to the response variable 'model error' [i.e., $x_{s,i} - x_{o,i}$, the difference in days calculated as the ~~simulated~~predicted minus the observed date for each stage and site-year (*i*)] in the validation sample (Sect. 2.6 and S2.3), based on 41 068 observations, and resulted in an adjusted R^2 of 0.44 and a proportion of the deviance explained of 0.44. The random intercepts were grouped by site with σ_b = 9.32 d (99% confidence interval $8.26 \leq \sigma_b \leq 10.52$ d). SE is the standard error, while 'Lower 0.05%' and 'Upper 99.5%' indicate the lower and upper boundaries of the 99% confidence interval. Bold *p*-values are indicate significant fixed effects at α = 0.01 (i.e., $p \leq 0.005$ for a two-sided hypothesis test), bold and italic minimum Bayes factors ($\underline{BF}_{01}$) indicate decisive and very strong fixed effects (i.e., $\underline{BF}_{01} \leq 1/1000$ and $\underline{BF}_{01} \leq 1/100$, respectively). The intercept represents the base line, i.e., the model error according to the Null model for the reference level Austria. CDD, DM2, PIA, and DP3 are the factorized models, while SUI, GER, and GBR are the factorized countries Switzerland, Germany, and Great Britain, respectively. The random intercepts were grouped by 'site'. All models ware calibrated and validated with the LS$_{50}$ sample (Sect. 2.4).

Table S10. Interacting effects according to the LMM

Variable	Model	Country	Estimate	SE	0.5 %	99.5 %	Equation
Country [d]	Null	AUT	8.11	1.53	4.17	12.05	β_0
		SUI	2.01	1.50	−1.86	5.87	β_0 + SUI
		GER	0.28	1.34	−3.16	3.73	β_0 + GER
		GBR	−16.52	2.02	−21.71	−11.32	β_0 + GBR
	CDD	AUT	6.30	1.55	2.31	10.28	β_0 + CDD
		SUI	0.19	1.52	−3.72	4.11	β_0 + CDD + SUI
		GER	−1.53	1.33	−4.96	1.90	β_0 + CDD + GER
		GBR	−18.33	2.00	−23.49	−13.17	β_0 + CDD + GBR
	DM2	AUT	7.38	1.55	3.39	11.36	β_0 + DM2
		SUI	1.27	1.52	−2.64	5.18	β_0 + DM2 + SUI
		GER	−0.45	1.33	−3.88	2.98	β_0 + DM2 + GER
		GBR	−17.25	2.00	−22.41	−12.09	β_0 + DM2 + GBR
	PIA	AUT	7.48	1.52	3.56	11.41	β_0 + PIA
		SUI	1.38	1.49	−2.47	5.23	β_0 + PIA + SUI
		GER	−0.35	1.36	−3.84	3.15	β_0 + PIA + GER
		GBR	−17.15	2.04	−22.40	−11.89	β_0 + PIA + GBR
	DP3$_{LS_{50}}$	AUT	8.21	1.55	4.23	12.20	β_0 + DP3$_{LS_{50}}$
		SUI	2.11	1.52	−1.80	6.02	β_0 + DP3$_{LS_{50}}$ + SUI
		GER	0.39	1.33	−3.05	3.82	β_0 + DP3$_{LS_{50}}$ + GER
		GBR	−16.41	2.00	−21.57	−11.25	β_0 + DP3$_{LS_{50}}$ + GBR
δELV [d 100 m^{-1}]	Null	AC	1.13	0.31	0.34	1.93	100 δELV
	CDD		1.01	0.32	0.20	1.83	100 (δELV + CDD × δELV)
	DM2		1.02	0.32	0.20	1.84	100 (δELV + DM2 × δELV)
	PIA		1.00	0.32	0.18	1.82	100 (δELV + PIA × δELV)
	DP3$_{LS_{50}}$		1.14	0.32	0.32	1.95	100 (δELV + DP3$_{LS_{50}}$ × δELV)
δLAT [d °N^{-1}]	Null		2.11	0.47	0.90	3.33	δLAT
	CDD		2.06	0.48	0.82	3.29	δLAT + CDD × δLAT
	DM2		2.05	0.48	0.81	3.28	δLAT + DM2 × δLAT
	PIA		2.08	0.48	0.84	3.31	δLAT + PIA × δLAT
	DP3$_{LS_{50}}$		2.13	0.48	0.90	3.36	δLAT + DP3$_{LS_{50}}$ × δLAT
δMAQ [d 100^{-1}]	Null		9.01	1.79	4.38	13.63	100 δMAQ
	CDD		3.63	2.29	−2.28	9.54	100 (δMAQ + CDD × δMAQ)
	DM2		3.98	2.29	−1.93	9.89	100 (δMAQ + DM2 × δMAQ)
	PIA		4.27	2.37	−1.83	10.37	100 (δMAQ + PIA × δMAQ)
	DP3$_{LS_{50}}$		7.54	2.29	1.63	13.45	100 (δMAQ + DP3$_{LS_{50}}$ × δMAQ)
δMAT [d 10°C^{-1}]	Null		−20.03	1.31	−23.39	−16.66	10 δMAT
	CDD		−21.49	1.69	−25.84	−17.13	10 (δMAT + CDD × δMAT)
	DM2		−21.80	1.69	−26.16	−17.44	10 (δMAT + DM2 × δMAT)
	PIA		−19.07	1.69	−23.43	−14.71	10 (δMAT + PIA × δMAT)
	DP3$_{LS_{50}}$		−20.46	1.69	−24.82	−16.10	10 (δMAT + DP3$_{LS_{50}}$ × δMAT)
δA_{net} [d 10 mol C^{-1} m^{-2}]	Null		4.15	0.16	3.74	4.56	10 δA_{net}
	CDD		4.32	0.21	3.78	4.86	10 (δA_{net} + CDD × δA_{net})
	DM2		4.24	0.21	3.70	4.78	10 (δA_{net} + DM2 × δA_{net})
	PIA		4.61	0.21	4.08	5.15	10 (δA_{net} + PIA × δA_{net})
	DP3$_{LS_{50}}$		4.12	0.21	3.58	4.65	10 (δA_{net} + DP3$_{LS_{50}}$ × δA_{net})

Note: The interacting effects of the LMM (Table S9) were calculated with the Delta method (Chpt. 5.1.4 in Fox and Weisberg, 2019; Chpt. 9.9 in Wasserman, 2004) according to the displayed equation, together with their standard error (SE) and 99% confidence interval (i.e., the 0.5% lower bound and 99.5% upper bound). AUT, SUI, GER, and GBR refer to the countries Austria, Switzerland, Germany, and Great Britain, respectively, while AC marks estimates across countries. The unit for δA_{net} is d 10 mol C^{-1} m^{-2}.

Table S11. Impact on the variance in the model error explained by the LMM

Explanatory variable	Impact	Accumulated	*p*-value	BF$_{01}$
Site	0.9164	0.9164	**0.0000**	**0.0000**
δA_{net}	0.0591	0.9755	**0.0000**	**0.0000**
δMAT	0.0195	0.9950	**0.0000**	**0.0000**
Model	0.0032	0.9982	**0.0000**	**0.0000**
δMAQ	0.0011	0.9993	**0.0000**	**0.0000**
Model × δMAQ	0.0003	0.9996	0.1799	0.8997
Model × δA_{net}	0.0002	0.9998	0.3213	1.0000
Model × δMAT	0.0001	0.9999	0.7026	1.0000
Model × δELV	0.0001	1.0000	0.7110	1.0000
δLAT	0.0000	1.0000	**0.0000**	**0.0000**
δELV	0.0000	1.0000	**0.0000**	**0.0000**
Country	0.0000	1.0000	**0.0000**	**0.0000**
Model × δLAT	0.0000	1.0000	0.9770	1.0000

Note: The type-III analysis of variance (ANOVA; Sect. 2.6 and S2.3) was based on the LMM (Table S9) and thus on 54 834 observations. For each explanatory variable (i.e., fixed and random effects), the impact on the variance in the model error as explained by the LMM is given, together with the accumulated impact when ordered by impact. Bold *p*-values are significant at α = 0.01 (i.e., $p \leq 0.01$ for a one-sided hypothesis test) and bold minimum Bayes factors (BF$_{01}$) are decisive (i.e., $\underline{BF_{01}} \leq 1/1000$).

References

Akaike, H.: A new look at the statistical model identification, IEEE Trans. Autom. Control, 19, 716–723, https://doi.org/10.1109/TAC.1974.1100705, 1974.

Baayen, R. H., Davidson, D. J., and Bates, D. M.: Mixed-effects modeling with crossed random effects for subjects and items, J. Mem. Lang., 59, 390–412, https://doi.org/10.1016/j.jml.2007.12.005, 2008.

Brock, T. D.: Calculating solar radiation for ecological studies, Ecol. Model., 14, 1–19, https://doi.org/10.1016/0304-3800(81)90011-9, 1981.

Burnham, K. P. and Anderson, D. R.: Multimodel Inference: Understanding AIC and BIC in Model Selection, Sociol. Methods Res., 33, 261–304, https://doi.org/10.1177/0049124104268644, 2004.

Candelieri, A.: A gentle introduction to Bayesian Optimization, 2021 Winter Simulation Conference (WSC), Phoenix, AZ, and virtual, 1–16, https://doi.org/10.1109/WSC52266.2021.9715413, 2021.

Collatz, G. J., Ball, J. T., Grivet, C., and Berry, J. A.: Physiological and environmental-regulation of stomatal conductance, photosynthesis and transpiration - A model that includes laminar boundary-layer, Agric. For. Meteorol., 54, 107–136, https://doi.org/10.1016/0168-1923(91)90002-8, 1991.

Farquhar, G. D., von Caemmerer, S., and Berry, J. A.: A biochemical model of photosynthetic CO_2 assimilation in leaves of C3 species, Planta, 149, 78–90, https://doi.org/10.1007/bf00386231, 1980.

Fisher, R. A. and Russell, E. J.: On the mathematical foundations of theoretical statistics, Philos. Trans. R. Soc. Lond. Ser. Contain. Pap. Math. Phys. Character, 222, 309–368, https://doi.org/10.1098/rsta.1922.0009, 1997.

Foster, G. R., McCool, D. K., Renard, K. G., and Moldenhauer, W. C.: Conversion of the universal soil loss equation to SI metric units, J. Soil Water Conserv., 36, 355–359, 1981.

Fox, J. and Weisberg, S.: An R Companion to Applied Regression, Third., SAGE, Los Angeles, 2019.

Geodesy: Approximate formulas for the transformation between Swiss projection coordinates and WGS84, 2016.

Gerten, D., Schaphoff, S., Haberlandt, U., Lucht, W., and Sitch, S.: Terrestrial vegetation and water balance - hydrological evaluation of a dynamic global vegetation model, J. Hydrol., 286, 249–270, https://doi.org/10.1016/j.jhydrol.2003.09.029, 2004.

Gupta, H. V., Kling, H., Yilmaz, K. K., and Martinez, G. F.: Decomposition of the mean squared error and NSE performance criteria: Implications for improving hydrological modelling, J. Hydrol., 377, 80–91, https://doi.org/10.1016/j.jhydrol.2009.08.003, 2009.

Haxeltine, A. and Prentice, I. C.: BIOME3: An equilibrium terrestrial biosphere model based on ecophysiological constraints, resource availability, and competition among plant functional types, Glob. Biogeochem. Cycles, 10, 693–709, https://doi.org/10.1029/96gb02344, 1996.

Haxeltine, A., Prentice, I. C., and Creswell, D. I.: A coupled carbon and water flux model to predict vegetation structure, J. Veg. Sci., 7, 651–666, https://doi.org/10.2307/3236377, 1996.

Keetch, J. J. and Byram, G. M.: A Drought Index for Forest Fire Control, Department of Agriculture, Forest Service, Southeastern Forest Experiment Station, Asheville, NC: U.S., 1968.

Kling, H., Fuchs, M., and Paulin, M.: Runoff conditions in the upper Danube basin under an ensemble of climate change scenarios, J. Hydrol., 424–425, 264–277, https://doi.org/10.1016/j.jhydrol.2012.01.011, 2012.

Kloos, S., Klosterhalfen, A., Knohl, A., and Menzel, A.: Decoding autumn phenology: Unraveling the link between observation methods and detected environmental cues, Glob. Change Biol., 30, e17231, https://doi.org/10.1111/gcb.17231, 2024.

Lu, X. and Keenan, T. F.: No evidence for a negative effect of growing season photosynthesis on leaf senescence timing, Glob. Change Biol., 28, 3083–3093, https://doi.org/10.1111/gcb.16104, 2022.

Maes, F., Wehenkel, L., and Ernst, D.: Meta-learning of exploration/exploitation strategies: The Multi-armed bandit case, Agents and Artificial Intelligence, 100–115, 2013.

Meier, M. and Bigler, C.: Process-oriented models of autumn leaf phenology: ways to sound calibration and implications of uncertain projections, Geosci. Model Dev., 16, 7171–7201, https://doi.org/10.5194/gmd-16-7171-2023, 2023.

Swiss phenology network: https://www.meteoswiss.admin.ch/weather/measurement-systems/land-based-stations/swiss-phenology-network.html, last access: 29 January 2025.

Pinheiro, J. C. and Bates, D. M.: Mixed-effects models in S and S-PLUS, Springer, New York, 528 S. pp., 2000.

R Core Team: R: A language and environment for statistical computing, 2025.

Shaw, H. G.: Centigrade-Fahrenheit temperature conversion, J. Chem. Educ., 8, 727, 1931.

Sitch, S., Prentice, I. C., Smith, B., Cramer, W., Kaplan, J. O., Lucht, W., Sykes, M. T., Thonicke, K., and Venevsky, S.: LPJ - A Coupled Model Of Vegetation Dynamics And The Terrestrial Carbon Cycle. https://www.researchgate.net/publication/37456884, 2000.

Wang, H., Gao, C., and Ge, Q.: Low temperature and short daylength interact to affect the leaf senescence of two temperate tree species, Tree Physiol., 42, 2252–2265, https://doi.org/10.1093/treephys/tpac068, 2022.

Wasserman, L.: All of Statistics. A Concise Course in Statistical Inference, 1st ed., Springer New York, NY, 2004.

Wohlfahrt, G. and Gu, L.: The many meanings of gross photosynthesis and their implication for photosynthesis research from leaf to globe, Plant Cell Environ., 38, 2500–2507, https://doi.org/10.1111/pce.12569, 2015.

Wood, S. N.: Fast stable restricted maximum likelihood and marginal likelihood estimation of semiparametric generalized linear models, J. R. Stat. Soc. Ser. B Stat. Methodol., 73, 3–36, https://doi.org/10.1111/j.1467-9868.2010.00749.x, 2011.

Wood, S. N.: Generalized additive models: An introduction with R, 2nd edition., Chapman and Hall/CRC, New York, 2017.

Woods, H. W.: Centigrade-fahrenheit temperature conversion, J. Chem. Educ., 8, 370, 1931.

Xiang, Y., Sun, D. Y., Fan, W., and Gong, X. G.: Generalized Simulated Annealing algorithm and its application to the Thomson model, Phys. Lett. A, 233, 216–220, https://doi.org/10.1016/s0375-9601(97)00474-x, 1997.

Xiang, Y., Gubian, S., and Martin, F.: Generalized Simulated Annealing, in: Computational Optimization in Engineering - Paradigms and Applications, 25–46, 2017.

Yates, F.: The analysis of multiple classifications with unequal numbers in the different classes, J. Am. Stat. Assoc., 29, 51–66, https://doi.org/10.2307/2278459, 1934.

Zani, D., Crowther, T. W., Mo, L., Renner, S. S., and Zohner, C. M.: Increased growing-season productivity drives earlier autumn leaf senescence in temperate trees, Science, 370, 1066–1071, https://doi.org/10.1126/science.abd8911, 2020.